

Sunquake with a second bounce, other sunquakes, and emission associated with the X9.3 flare of 6 September 2017. I. Observations

Sergei Zharkov¹, Sarah Matthews², Valentina Zharkova³, Malcolm Druett⁴, Satoshi Inoue⁵, Ingolf E. Dammasch⁶, and Connor Macrae¹

¹ E.A.Milne Centre for Astrophysics, School of Mathematics and Physical Sciences, Hull University, Kingston upon Hull, HU6 7RX, United Kingdom

² UCL Mullard Space Science Laboratory, Holmbury St. Mary, Dorking, Surrey, RH5 6NT, United Kingdom

³ Northumbria University, Department of Mathematics, Physics and Electrical Engineering, Newcastle upon Tyne, NE1 8ST, United Kingdom

⁴ Stockholm University, Department of Astronomy, SE-106 91 Stockholm, Sweden,

⁵ Institute for Space–Earth Environmental Research (ISEE), Nagoya University, Furo-cho, Chikusa-ku, Nagoya, Japan, 464 8601

⁶ Royal Observatory of Belgium, Solar Influences Data Analysis Center, Circular Avenue 3, 1180 Uccle, Brussels, Belgium

May 7, 2020

Abstract. The 6 September 2017 X9.3 solar flare produced very unique observations of magnetic field transients and a few seismic responses, or sunquakes, detected by the Helioseismic and Magnetic Imager (HMI) instrument aboard Solar Dynamic Observatory (SDO) spacecraft, including the strongest sunquake ever reported. This flare was one of a few flares occurring within a few days or hours in the same active region. Despite numerous reports of the fast variations of magnetic field, and seismic and white light emission, no attempts were made to interpret the flare features using multi-wavelength observations. In this study, we attempt to produce the summary of available observations of the most powerful flare of the 6 September 2017 obtained using instruments with different spatial resolutions (Paper 1) and to provide possible interpretation of the flaring events, which occurred in the locations of some seismic sources (Paper 2). We employed non-linear force-free field (NLFFF) extrapolations followed by magnetohydrodynamic simulations in order to identify the presence of several magnetic flux ropes prior to the initiation of this X9.3 flare. Sunquakes were observed using the directional holography and time–distance diagram detection techniques. The high-resolution method to detect the $H\alpha$ line kernels in the CRISP instrument at the diffraction level limit was also applied. We explore the available gamma-ray (GR), hard X-ray (HXR), Lyman- α , and extreme ultra-violet (EUV) emission for this flare comprising two flaring events observed by space- and ground-based instruments with different spatial resolutions. For each flaring event we detect a few seismic sources, or sunquakes, using Dopplergrams from the HMI/SDO instrument coinciding with the kernels of $H\alpha$ line emission with strong redshifts and white light sources. The properties of sunquakes were explored simultaneously with the observations of HXR (with KONUS/WIND and the Reuven Ramaty High Energy Solar Spectroscopic Imager (RHESSI) payload), EUV (with the Atmospheric Imaging Assembly (AIA)/SDO and the EUV Imaging Spectrometer (EIS) aboard Hinode payload), $H\alpha$ line emission (with the CRisp Imaging Spectro-Polarimeter (CRISP) in the Swedish Solar Telescope (SST)), and white light emission (with HMI/SDO). The locations of sunquake and $H\alpha$ kernels are associated with the footpoints of magnetic flux ropes formed immediately before the X9.3 flare onset. For the first time we present the detection of the largest sunquake ever recorded with the first and second bounces of acoustic waves generated in the solar interior, the ripples of which appear at a short distance of 5-8 Mm from the initial flare location. Four other sunquakes were also detected, one of which is likely to have occurred 10 minutes later in the same location as the largest sunquake. Possible parameters of flaring atmospheres in the locations with sunquakes are discussed using available temporal and spatial coverage of hard X-ray, gamma-ray, EUV, hydrogen $H\alpha$ -line, and white light emission in preparation for their use in an interpretation to be given in Paper 2.

Key words. Sun: flares, Sun: X-rays, gamma-rays, Sun: helioseismology, radiative transfer, hydrodynamics

1. Introduction

Send offprint requests to: v.zharkova
valentina.zharkova@northumbria.ac.uk

e-mail: The complex processes of plasma heating in solar flares are associated with a primary release of magnetic energy via mag-

netic reconnection occurring in the corona (Priest & Forbes 2000; Somov 2000) and subsequent acceleration of energetic particles (Vilmer et al. 2011; Zharkova et al. 2011) precipitating along newly reconnected field lines (Holman et al. 2011; Kontar et al. 2011). These processes happen on a very short timescale during flare onset and can be effectively diagnosed from the increase of intensities in flaring emission of hard X-rays (HXR), γ -rays (GR), soft X-rays (SXR), extreme ultraviolet (EUV), ultra-violet (UV), microwave (MW), and optical emission (Zharkova 2008; Matthews et al. 2015, and references therein). Energetic electron beams precipitating into the flaring atmosphere (Brown 1971; Syrovatskii & Shmeleva 1972) can account for HXR and MW emission (Holman et al. 2011; Kontar et al. 2011) while proton and ion beams (Vilmer et al. 2011) can account for observed γ -ray emission. The scenarios by which the magnetic field is reconfigured while triggering flaring events and converting the energy of magnetic field into radiation and macro-motions in flares are to a large extent defined by the initial magnetic field topologies of interacting loops and the trigger mechanisms that initiate the reconnection process in each flaring case (Priest & Forbes 2000; Somov 2000).

Soft X-ray emission caused by the ambient plasma heating by particle beams produces emission in highly ionised elements, including for example Fe XXIV and Fe XXV ions (Porquet et al. 2001; Kawate et al. 2016), and often shows a longer (hours) duration. Furthermore, there are observed blueshifts in SXR and EUV emission with upward velocities of up to $1000 \text{ km}\cdot\text{s}^{-1}$ (Antonucci et al. 1982; Milligan et al. 2006a,b; Del Zanna 2008; Milligan & Dennis 2009; Polito et al. 2016). In addition, observations of Lyman- α lines by the instruments with low spatial resolution show impulsive brightening of Lyman line emission and the appearance of either red or blue wing asymmetries at different times of flare development (Procházka et al. 2017; Druett & Zharkova 2018; Dominique et al. 2018). This is also supported by brightening in Lyman continuum intensity, which becomes greatly enhanced from the continuum head at $\lambda = 910 \text{ \AA}$ along the other wavelengths (Kleint et al. 2016; Druett & Zharkova 2019), resulting in strong intensity flattening over the continuum wavelengths reported from observations (Machado et al. 2018; Druett & Zharkova 2019).

Simultaneously, with HXR bursts, gamma rays, SXR, and EUV emission growth, the dynamics of flares in the lower atmosphere can be effectively derived from the observations of optical lines and, in particular, hydrogen H α line 6563 \AA emission revealing large redshifts up to $4\text{-}5 \text{ \AA}$ (Ichimoto & Kurokawa 1984; Canfield & Gayley 1987; Zarro et al. 1988; Wuelser & Marti 1989), followed at later times by blueshifts as observed in stellar flares (Houdebine et al. 1990; Houdebine & Doyle 1994). In addition, notable increases in white light (WL, or Paschen continuum) emission (Uchida & Hudson 1972; Kurokawa et al. 1988; Matthews et al. 2011; Procházka et al. 2018), Balmer and near-UV continuum emission (Kleint et al. 2016; Kotřč et al. 2016; Druett & Zharkova 2018; Procházka et al. 2018) are often observed during early phases of flares. The locations of WL or Balmer continuum emission are nearly co-spatial with the contours of HXR emission and have close

depths of formation in flaring atmospheres (Druett & Zharkova 2018). Uchida & Hudson (1972) suggested that energetic electron beams injected into a flaring atmosphere can account for the temporal correlation of HXR and WL emission. Later, Aboudarham & Henoux (1987) proposed that WL emission can be mainly produced by negative hydrogen ions at very deep dense photospheric levels. However, the precise mechanisms responsible for the enhancement of WL emission in flares has remained an active topic for debate for three decades. Only recently, Druett & Zharkova (2018) showed that non-thermal ionisation of hydrogen atoms by relativistic electron beams can naturally produce strong increases in Balmer and Paschen (WL) emission during flares at chromospheric levels expanding from photospheric depths where this emission is expected to originate in the quiet Sun.

In addition, particle beams cause a large increase in collisional ionisation and excitation of hydrogen atoms by non-thermal electrons, which strongly (by orders of magnitude) increases excitation and the ionisation degree of hydrogen atoms from all atomic levels (Zharkova & Kobylinskii 1993). These non-thermal collisions combined with plasma heating caused by beam electrons can lead to an increase in hydrogen line and continuum radiation in Lyman, Balmer and Paschen series. This suggestion was recently tested with detailed radiative hydrodynamic simulations using the HYDRO2GEN code including non-thermal excitation and ionisation by beam electrons (Druett et al. 2017; Druett & Zharkova 2018, 2019). The authors confirmed the enhancement of Lyman, Balmer, and Paschen lines and continua of hydrogen atoms in flares caused by beam electrons. Druett & Zharkova (2019) showed that after the beam is switched off, the high ionisation degree of a flaring plasma gained during the beam injection is sustained for a very long time by Lyman continuum emission because of its large opacity. This leads to a long enhancement of hydrogen ionisation in the flaring atmosphere and an increase of the Lyman- α and β line emission in the line cores and wings. The earlier wide-spectral filter observations with large ($2\text{-}4 \text{ \AA}$) red shifts (e.g. Ichimoto & Kurokawa 1984; Wuelser & Marti 1989) cannot be seen by modern instruments with narrow ($2\times 1.5 \text{ \AA}$) spectral windows (Druett et al. 2017; Druett & Zharkova 2018), which explains the frequently reported delays of the order of 30 s between maximum HXR emission and the appearance of H α -line emission in powerful flares (Kaempfer & Magun 1983; Veronig et al. 2002; Radziszewski et al. 2011).

Strong, high-energy emissions in HXR, EUV, UV, and WL wavelengths are often accompanied by the occurrence of sunquakes or ripples on the solar surface radially emanating from a point source from 20-60 minutes after a flare onset (Kosovichev & Zharkova 1998; Zharkova & Zharkov 2007; Zharkova 2008; Donea 2011; Zharkov et al. 2011a; Zharkov et al. 2011b; Matthews et al. 2015). Sunquakes are detected on the solar surface using time–distance (TD) diagram analysis (Kosovichev & Zharkova 1998) and acoustic holography (Donea et al. 1999; Lindsey & Braun 1999; Donea et al. 2000; Lindsey & Braun 2000; Donea & Lindsey 2005). The sunquake origin is normally indicated by a compact bright kernel (source) peaking during a flare, which is verified by statistical tests (Zharkov et al. 2011a). Sunquakes have been detected in X-class (see,

e.g. Kosovichev & Zharkova 1998; Zharkova & Zharkov 2007; Moradi et al. 2007), M-class (Donea et al. 2006), and even in C-class (Sharykin et al. 2015) flares, while the most powerful sunquakes appeared to be associated with M-class flares (Donea 2011). The ripples are suggested (Kosovichev & Zharkova 1998; Zharkov 2013) to be reflections from the solar surface of acoustic (in some cases, magneto-acoustic) waves induced by a sharp deposition into the solar interior of the momentum delivered by hydrodynamic shocks formed in flaring atmospheres. Some localised magnetic configurations are found to be more effective in channeling the energy and momentum to the lower atmosphere (Green et al. 2017).

The mechanisms responsible for the generation of sunquakes are still under investigation. The first of the mechanisms proposed for generating sunquakes was a hydrodynamic response of flaring atmospheres to the injection of energetic particle beams (Kosovichev & Zharkova 1998; Zharkov 2013; Macrae et al. 2018), which produces strong hydrodynamic shocks travelling downward to photospheric levels at supersonic speed (Somov et al. 1981; Fisher et al. 1985c,a; Allred et al. 2005; Zharkova & Zharkov 2007; Zharkova & Zharkov 2015). Some authors have also suggested radiative backwarming as a source of pressure transients that can produce acoustic waves (Donea et al. 2006; Donea 2011). However, observations show that some sunquake locations are associated with little or no white light emission, and little or no HXR emission (Matthews et al. 2011; Buitrago-Casas et al. 2015; Zharkov et al. 2011a). Hudson et al. (2008); Fisher et al. (2012) noted that sunquakes often occur in the locations of Lorentz force transients, which can produce a well-directed magnetic impulse of Poynting vector towards the photosphere and subsequent magneto-acoustic wave conversion (Cally 2006; Hansen et al. 2016).

Recently, Macrae et al. (2018) detected a sunquake in the flare of 6 September 2011, which was previously reported to be acoustically inactive (Liu et al. 2014). Subsequently, the authors (Macrae et al. 2018) provided a quantitative interpretation of the properties of the sunquake (timing, directionality) using a hydrodynamic model for plasma heating by beam electrons as an input for the hydrodynamic model for acoustic wave propagation in the solar interior. They demonstrated that all three mechanisms associated with the generation of seismic signatures are present in flaring atmospheres if they have sunquakes. The energetic particles gain their energy from a reconnecting current sheet formed during a flare by converting the magnetic energy into particles with the help of Lorentz force. Also, the same relativistic electrons over-ionise the ambient hydrogen plasmas by five to six orders of magnitude and keep it in this state for a very long time for up to 40 minutes by the radiative transfer in optically thick Lyman continuum (Druett & Zharkova 2019) leading to the appearance of white light emission (Druett & Zharkova 2018).

On 6 September 2017 the active region NOAA 12673 produced two X-class flares: an X2.2 flare and three hours later an X9.3 flare, which have been studied by many authors. A few sunquakes associated with the X9.3 flare were originally reported by Sharykin & Kosovichev (2018). Further helioseismic analyses of magneto-acoustic waves in this active region

were carried by Zhao & Chen (2018), who also discovered fast and slow magneto-acoustic waves that occurred prior to the major sunquakes and travelled through this active region. Similar waves were also seen in Ca II line spectral observations by the Swedish Solar Telescope (SST), as recently reported by Quinn et al. (2019), who linked these Ca II waves to the largest sunquake. Keeping in mind that maximum Doppler velocities of the first bounce of these acoustic waves formed in the interior measured from the HMI dopplergrams do not exceed of ± 3 km/s at the photosphere as reported in Fig. 2 by Sharykin & Kosovichev (2018), it is important to establish, whether these or other waves can reach the heights of the chromosphere to produce the Ca II waves seen by Quinn et al. (2019). Alternatively, these chromospheric Ca II waves may be linked to the slow magneto-acoustic waves seen in the HMI dopplergrams prior the sunquake onsets as reported by Zhao & Chen (2018).

Both flares produced very extensive white light emission in the shape of ribbons (Romano et al. 2018). All authors reported a complex magnetic structure for the active region and the non-linear force-free field (NLFFF) reconstruction of the magnetic field in this active region prior to the X2.2 flare. In order to restore magnetic configuration at the start of X9.3 flare, three-dimensional MHD simulations were carried out (Inoue et al. 2018) revealing that there were three magnetic flux ropes (MFRs) formed after the X2.2 flare and just prior to the X9.3 flare. These MFRs are very likely to be associated with sunquakes as discovered earlier by Zharkov et al. (2011a); Green et al. (2017).

In this paper we aim to compare available multi-wavelength observations and multiple sunquakes in the flare of 6 September 2017 and to summarise the observed parameters of flaring atmospheres linked to detected sunquakes in order to provide a basis for their interpretation by the radiative hydrodynamic model HYDRO2GEN. The flare location and available high-energy observations are discussed in section 2, seismic observations of this flare are reported in section 3, and extra ultra-violet (EUV) and optical observations in the H α line and white light emission are described in section 4. Derived parameters in the locations of sunquakes are discussed in section 5 and the general implications of the differences in temporal and spatial resolutions for the possible interpretation of the results in paper 2 are discussed in section 6.

2. Active region and high-energy emission

2.1. Active region and magnetic field evolution

NOAA active region (AR) 12673 was a flare-prolific region that had one of the fastest magnetic flux emergence rates ever observed (Inoue et al. 2018). The AR became very active from September 4, 2017, and produced many C- and M-class flares over a time interval of two days, eventually resulting in the production of an X2.2 flare at 08:57 UT and an X9.3 flare at 11:56 UT (SOL2017-09-06T11:53) on September 6 at disc location S09W34.

The non-linear force-free field (NLFFF) restoration of the magnetic field in this active region prior to the X2.2 flare fol-

lowed by 3-dimensional (3D) magneto-hydrodynamic (MHD) simulations of magnetic field dynamics during the recent two solar flaring events of X-class occurred on 6 September 2017 (Inoue et al. 2018) revealed that after the X2.2 flare and prior to the X9.3 flare three magnetic flux ropes (MFRs) formed with very braided and twisted magnetic structures. It was shown that a tether cutting reconnection between the red and green loops illustrated in the left plot of Fig. 1 produced long twisted red magnetic lines and drove the eruption during the X9.3 flare. Furthermore, the right plot of Fig. 1 shows the MHD simulations of the red and green loop interaction where one footpoint of this red loop became anchored in the positive polarity and the another footpoint was embedded in the negative polarity located in the northern area away from the main part of the active region. These long twisted red lines eventually reconnected with the green and blue lines creating a large green flux rope, which erupted during the X9.3 flare. The places where the ropes are embedded into the photosphere are close to the locations of the sunquakes reported in section 3.

2.2. γ - and hard X-ray bremsstrahlung emission observed by KONUS/WIND

The top plot of Fig. 2 shows the light curves of the flare emission at soft X-ray (SXR) emission by the Geostationary Operational Environmental Satellite (GOES) and γ -ray emission by the Gamma Ray Burst Detector (KONUS) payload aboard WIND satellite (Aptekar et al. 1995) in flaring event 1 (FE1). The middle plot of Fig. 2 shows the light curves of Ly- α line taken by the Large-Yield RADIometer (LYRA) (Hochedez et al. 2006) in flaring events 1 and 2 (FE1 and FE2); while the bottom plot presents the HXR light curve taken shortly after FE2 by the Reuven Ramaty High Energy Solar Spectroscopic Imager (RHESSI Lin et al. 2002).

Flaring event 1 (FE1) of the X9.3 flare of the 6 September, 2017, occurred at 11:55:29.0 UT. This flaring event, together with a few spikes, was observed by KONUS/WIND (see Fig.2a) and lasted for a few minutes before the second series of flaring events occurred from 12:04:30 UT to 12:07 UT, which were recorded in Ly α line emission by the LYRA payload (see section 2.3). The third flaring event starting from 12:08 UT was later recorded also by RHESSI (see section 2.4). The KONUS instrument aboard WIND satellite consists of two 13 cm x 7.5 cm NaI(Tl), which are located on the opposite faces of the Wind spacecraft, and observes the southern and the northern ecliptic hemispheres (Aptekar et al. 1995). The count rates were measured in three wide energy bands, G1 (20-80 keV), G2 (80-300 keV), and G3 (300-1200 keV). The time history in G1, G2, and G3 channels with high temporal resolution is available from 11:55:29.0 UT until 11:59:18.7 UT as shown in the top plot of Fig. 2 (Lysenko et al. 2019).

Multichannel spectral fitting in the 20 keV - 15 MeV energy range was carried out in nine time intervals. Bremsstrahlung continuum of HXR emission in the lower energy range demonstrates soft-hard-soft spectral evolution during the main flare peak. The time-integrated energy spectra obtained by KONUS are plotted in Fig.3. Proton spectral index in ≤ 30 MeV energy

range is $s = 4.0 \pm 1$ and the total energy of ions was estimated to be about 1.1×10^{31} erg (Lysenko et al. 2019). Temporal variations of the power-law energy spectra shown a soft-hard-soft pattern (for details, see the discussion, p.11, last paragraph in Lysenko et al. 2019). For the area of footpoints affected by this beam we considered H α line observations, which allowed us to estimate the initial energy flux of particle beams.

2.3. Lyman- α emission

The Large-Yield RADIometer (LYRA) is an instrument on the ESA microsatellite, the PROject for On-Board Autonomy (PROBA2), which is a combined technology, science, and space-weather mission in Sun-synchronous orbit at 725km altitude. LYRA has observed solar UV irradiance continuously since January 2010 in high cadence, and consists of three observation units, each with four spectral channels: channel 1 (120-123nm), channel 2 (190-222nm), channel 3 (0.1-80nm), and channel 4 (0.1-20nm) (for a detailed instrument description see Hochedez et al. 2006; Dominique et al. 2013).

In September 2017, when NOAA AR 12673 began to grow quickly, LYRA observed the following irradiance response to the X9.3 flare (Fig.2, middle plot): Channel 1 shows an increase of 0.97%, of which 70% is caused by the Ly- α residual; channel 2 shows an increase of 0.35%; channel 3 shows an increase of more than six times, and channel 4 of almost 17 times. The latter are still smaller than the GOES irradiance increase (192 times) because the GOES increase during the flare is 192 bigger than its pre-flare level, but not 192 times bigger than the LYRA increase.

The information in the middle plot of Fig. 2 demonstrates that the FUV/MUV flare signatures of channels 1 and 2 are non-thermal and coincide with the flaring event at 11:55:30 UT reported by KONUS (see section 2.2) in flaring event 1; these signatures follow the derivative of the GOES curve. In the beginning phase of the flare, these two channels rise almost in parallel. The further increase of Ly α emission during the next flare (flaring event 2) was recorded in SXR/EUV channels 3 and 4, which follow the GOES curve. These channels contain the GOES spectral interval on their short-wavelength side, but also lower- temperature signatures. Thus, the Ly α emission in channels 4 peaked slightly later and channel 3 peaked even later than channel 4. Therefore, the Ly- α light curve clearly demonstrates a succession of four distinct flaring events occurring at approximately 11:55:30 UT, 12:04 UT, 12:06:40 UT, and 12:08 UT. These events were seen separately by KONUS (FE1) and then by RHESSI (the last flaring event) payload as described in sections 2.2 and 2.4, respectively.

2.4. RHESSI hard X-ray emission

The RHESSI spacecraft (Lin et al. 2002) was passing through SAA during the onset and rise of the X9.3 flare, but began observing at 12:08 UT after the start of FE2 at 12:06:40 UT, with detectors 1, 3, 6, and 8 (see Fig. 2c). At the time of flaring event 2 (12:07 UT) there was no detectable HXR emission associated with the footpoints F1-F3 of the northern complex of the active

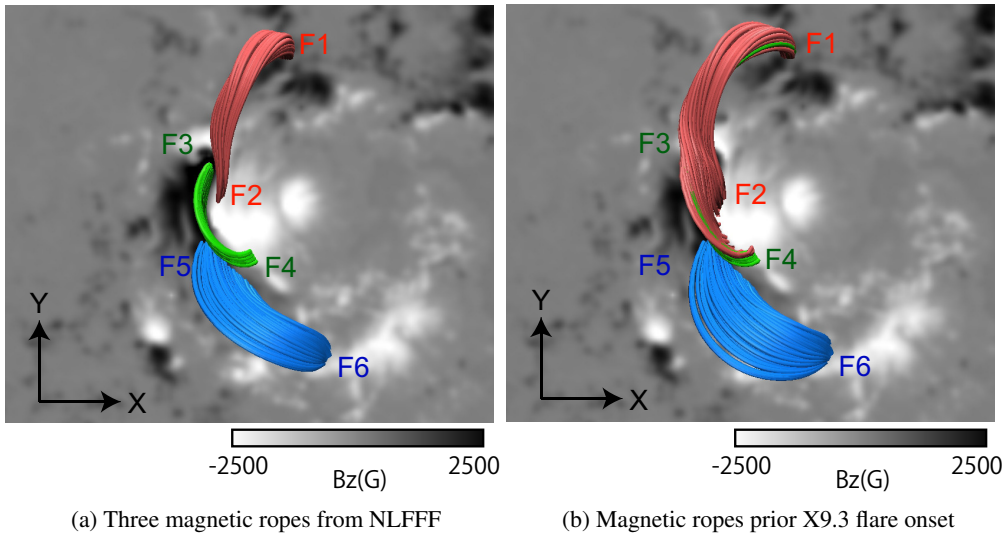


Fig. 1. Magnetic flux ropes formed during the X2.2 flare just prior to the 9.3 flare derived from NLFFF magnetic field reconstruction by Inoue et al. (2018) (a), which established the magnetic topology derived by the MHD simulations just prior to the X9.3 flare (b) with the loop footpoints being linked to the sunquake locations detected for this flare.

region. However, we were able to detect HXR emission in the central part of the active region near footpoint F4 and to derive parameters of the electron spectrum from detectors 3 and 8 between 12:08:00 and 12:08:08 UT, which was 1.2 minutes after the $H\alpha$ kernel was detected at 12:06:40 UT (see sections 4.1 and 4.2.1). For a simple demonstration, we reconstructed the HXR emission at 12:08 UT (after the onset of FE2) in the 30 - 60 keV range with the PIXON algorithm using detectors 1, 3, 6, and 8 and a 40 second accumulation time.

The RHESSI missed the impulsive phase of both FE1 and FE2 but recorded the emission during the last flaring event after 12:08 UT seen also in the $Ly\alpha$ light curve (Fig.2b; see section 2.3). The location of HXR emission is co-spatial with the location of $H\alpha$ line kernel3 in FE2, which points out some similarities between FE2 and the last flaring event; for example, the similar magnetic structures causing primary energy releases, which are sometimes referred to as sympathetic flares. The total energy of the observed HXR emission was approaching 10^{31} erg, which is comparable to that derived from KONUS data above for FE1. This energy was used to estimate the initial energy flux of electron/mixed beam supposedly producing FE2 in the location for $H\alpha$ kernel 3 by using the area of $H\alpha$ emission, as discussed in section 5 and Paper 2, on the basis that the FE2 and the flaring event seen by RHESSI had similar characteristics. This assumption can be tested during the interpretation of the $H\alpha$ line profile discussed in Paper 2 (Zharkova et al. 2020).

3. Detecting sunquakes

3.1. Method of detection

For detection of seismic sources, or sunquakes, associated with the flare, two techniques are applied to the dopplergrams: 1) Detection of ripples travelling from the flare by building a time–distance (TD) diagram and 2) gathering all the distur-

bances of the surface and locating their starting point using the acoustic holography method.

3.1.1. Time–distance diagram

Time–distance (TD) diagrams (Kosovichev & Zharkova 1998; Zharkov et al. 2011a; Zharkov et al. 2011b, 2013a,b) are used to measure and interpret the travel times of acoustic waves on the solar surface. They are computed by choosing a central point-source location, rewriting the observed velocity signal at the surface into polar co-ordinates, and then applying an azimuthal transformation as follows:

$$V_m(r, t) = \int_{\alpha}^{\beta} v(r, \theta, t) e^{im\theta} d\theta, \quad (1)$$

over a full circle or over a selected arc (if the ripples are directional). After about 20 seconds from a flare onset the surface wavefront can be seen as ripples travelling with an increasing speed from the flare site. In the TD diagram, the locations of ripples are plotted versus time, and this information is presented as a ridge describing the ripple appearance on the surface, which can be compared with a theoretical ray path. This ridge can be extrapolated back in time allowing for more precise determination of the onset time of the acoustic source. Not all flares show discernible ripples despite some of them still having seismic signatures detected with a helioseismic holography.

3.1.2. Acoustic holography

Helioseismic holography is the phase-coherent computational reconstruction of the acoustic field into the solar interior, which is used to produce stigmatic images of the subsurface sources generating the disturbance (Braun & Lindsey 2000). Central to calculating egression is the Green's function, which de-

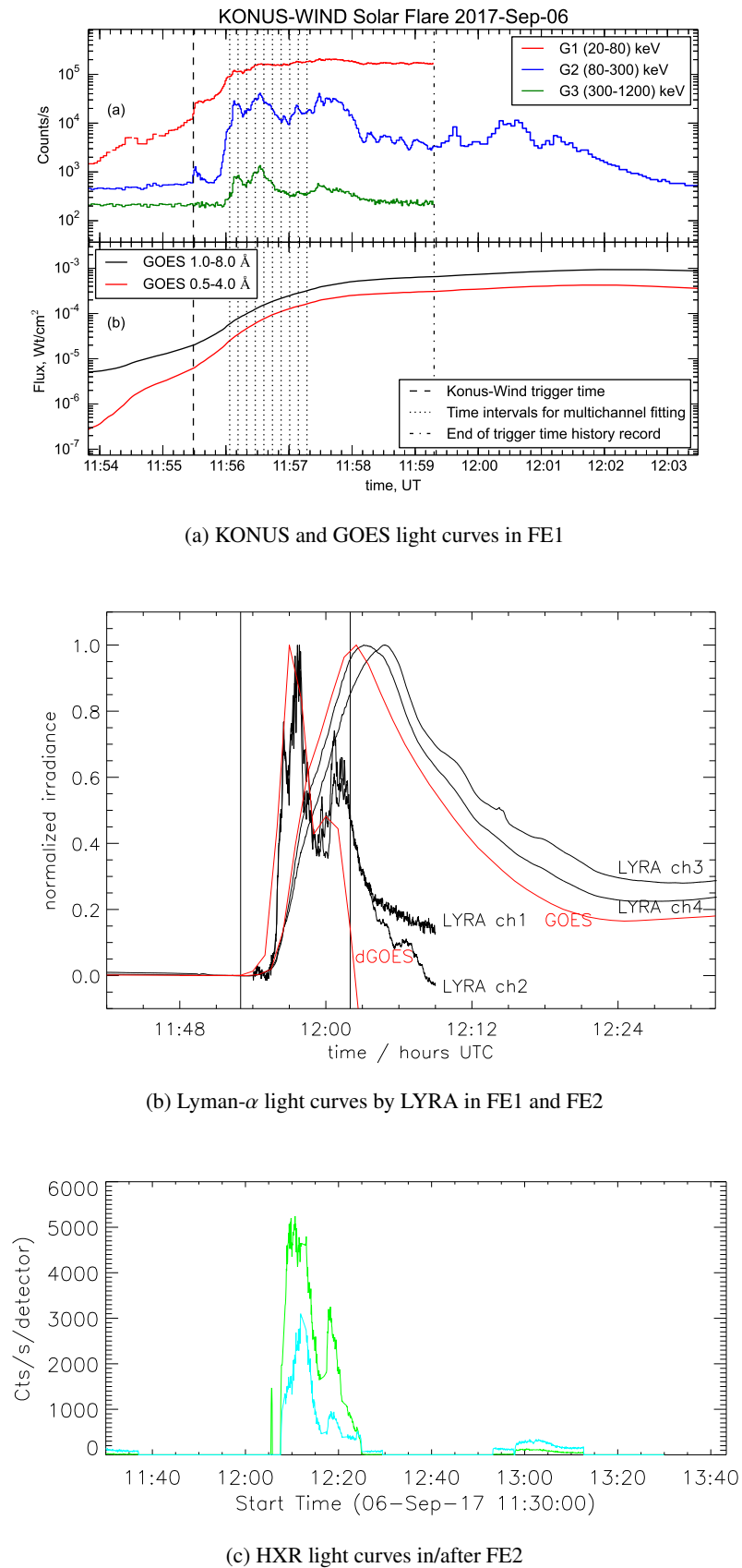


Fig. 2. The light curves of the X9.3 flare. a): Light curves by the KONUS instruments (upper plot) and by GOES (bottom plot). b): the light curve in Ly- α line observed by the LYRA instrument (Hochedez et al. 2006; Dominique et al. 2013) showing flaring events 1 (after 11:55 UT) and 2 (after 12:04 UT, see the text for details). c): the light curves of HXR emission during or after the flaring event 2 observed after 12:08 UT by RHESSI, Green line - 25 - 50 keV; Cyan line: 50 - 100 keV (scaled).

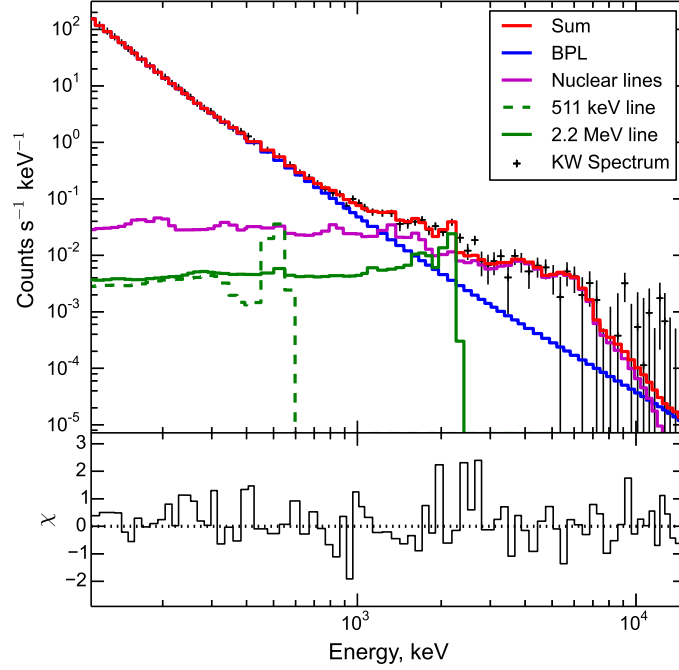
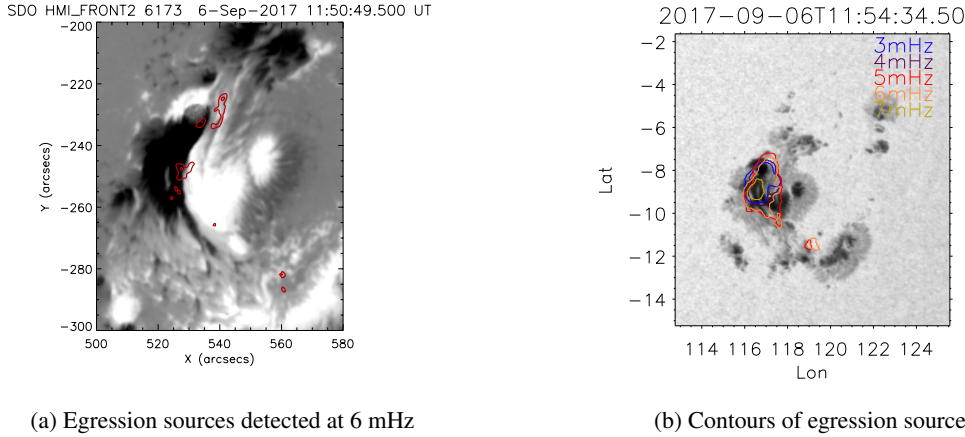


Fig. 3. Fitting of the time-integrated spectrum by the broken power law+NUCLEAR+511keV+2.2 MeV model (Lysenko et al. 2019). The component colour codes are given in the panel. The Konus/Wind (KW) data are shown using symbols, where the horizontal dashes indicate the energy range of each data point, while the vertical dashes indicate the corresponding statistical errors. The lower panel shows the fit residual. Adopted from Fig.3 of Lysenko et al. (2019).



(a) Egression sources detected at 6 mHz

(b) Contours of egression sources at 3-6 mHz

Fig. 4. (a) HMI magnetogram of the active region overplotted with egression maps at 6 mHz only. (b) Contours of the egression maps of sunquakes 1-4 in different frequencies marked by different colours over-imposed on the WL image.

describes acoustic wave propagation from a point source in order to backtrack the observed surface signal. Generally, these functions can be constructed through ray theory (Lindsey & Braun 2000; Zharkov et al. 2011a) for a monochromatic point source, as used in this work, or through wave theory (Lindsey & Braun 2004). Egression is calculated from the Green's function, $G_+(\mathbf{r} - \mathbf{r}', \nu)$, as follows in the temporal Fourier domain

(Zharkov et al. 2011a; Zharkov et al. 2013a,b):

$$\begin{aligned} \hat{H}_+(\mathbf{r}, \nu) &= \int_{a < |\mathbf{r} - \mathbf{r}'| < b} d^2\mathbf{r} G_+(\mathbf{r} - \mathbf{r}', \nu) \hat{\psi}(\mathbf{r}', \nu) \\ &= \int_0^{2\pi} d\theta \int_{a < r < b} dr G_+(\mathbf{r} - \mathbf{r}', \nu) \hat{\psi}(\mathbf{r}', \nu), \end{aligned} \quad (2)$$

where $\hat{\psi}(\mathbf{r}', \nu)$ represents the surface signal obtained from the HMI data, r and θ are polar coordinates around the sources as in (1), and a and b define the dimensions of the holographic pupil. Taking the inverse Fourier transform one obtains:

$$H_+(\mathbf{r}, t) = \int_{\Delta\nu} d\nu e^{2\pi i\nu t} \hat{H}_+(\mathbf{r}, \nu). \quad (3)$$

Egression power is then calculated by integrating the modulus squared over time as

$$P(\mathbf{r}, t) = \int |H_+(\mathbf{r}, t)|^2 dt. \quad (4)$$

Sunquakes are usually identified as localised enhanced emission spatially and temporally coincident with the flare, with the acoustic egression kernels usually derived on the egression power snapshots around the time of the flare, $P(\mathbf{r}, t_{\text{flare}})$, via a suitable threshold.

3.1.3. Directional holography

We use the method of directional holography, splitting the pupil into arcs (Macrae et al. 2018). In other words, the azimuthal angle θ integration in Eq. (2) between 0 and 2π is instead carried out over an arc of, for example, 0 to $\pi/2$. Dividing by the total power will then supply a fraction of egression power from acoustic waves that have travelled in the selected direction. Therefore, this allows for quantitative consideration of source anisotropy, or simply directional distribution of the acoustic power emitted from a source.

Helioseismic egression is computed from the single frame running difference SDO/HMI dopplergrams, with a pupil size of 10 – 80 Mm. Frequency ranges are chosen from the acoustic spectrum as 1 mHz bands, incrementally increasing from 2.5 – 3.5 mHz to 9.5 – 10.5 mHz, denoted hereafter the central frequency of each band. We note that the band size selection induces a limit to egression time resolutions of $\Delta t = 1/(1 \text{ mHz}) = 1000 \text{ s}$. To account for weak and dispersed sunquake sources that may be obscured by stochastic noise, even within acoustically damped sunspot features, we developed a reliable semi-automated statistical method allowing confident detection of a sunquake as follows:

1. Select a 21×21 pixel ($10.2 \times 10.2 \text{ Mm}$) box smoothing to the full datacube;
2. choose a flare time window in which to search for a signal, defined in such a way to enclose the flare's impulsive duration. This ensures the testing occurs only in the time frame where one expects a source to appear, and allows any strong signal to be excluded from the calculation of statistical parameters;
3. establish a boundary of 50 pixels (24.3 Mm) from each box edge so as to exclude the data input from the datacube edges, which can suffer from anomalies induced during the egression computation. As remapping is carried out to the centre of a flare location, this does not affect the resultant detections;
4. apply a signal-to-noise test with a threshold of 5σ to all the pixels within the selected datacube and in each frequency band. Through the analysis of known seismic events, we find a threshold of 5σ can only be exceeded by the acoustic signals driven by a flare impulse, and is rarely exceeded by the stochastic emission.

As a result, we expect that in the locations of sunquakes a significant signal in any frequency band will exceed the

5σ threshold above the local mean of the background signal (Zharkov et al. 2011a; Zharkov et al. 2011b). However, this is an insufficient definition, as occasionally we see stochastically driven noise (e.g. in the quiet sun) exceed this threshold in low-frequency bands (which are more susceptible to stochastic noise), thus creating some sporadic acoustic sources.

Therefore, we enforce a number of additional constraints for the seismic detection described below. Initially, for a proven seismic signal, we require a successful detection in the 6 mHz band. The lower end of the acoustic spectrum ($2 - 5 \text{ mHz}$) exhibits increased ambient noise due to convection (e.g. p-modes) which can compete unfavourably with acoustic emission (Donea et al. 2006). As the sub-photosphere is an effective specular reflector, low-frequency waves will undergo a number of surface skips whilst retaining coherency (Donea et al. 2000), meaning that emission in the vicinity of a pupil centre is in part comprised of p-mode energy reflection from elsewhere (Lindsey & Braun 1999). Conversely, at frequencies above 5 mHz , the quiet sun photosphere reflectivity becomes close to being a perfect absorber, thereby, inducing a limit of a single surface skip (Lindsey & Braun 1999; Donea et al. 2000).

In addition, the acoustic waves of these frequencies offer a finer diffraction limit and improved depth discrimination (Donea et al. 2000). Therefore, signals appearing in 6 mHz egression power images can be attributed as likely seismic sources, because of the decreased, p-mode induced, background noise level, which is lower by more than an order of magnitude (Donea & Lindsey 2005; Donea et al. 2006). Strong seismic events show kernel brightening across the acoustic spectrum. Therefore, we crucially expect further seismic signatures to be visible in the multiple frequency bands above and below this frequency of 6 mHz . Naturally, these detections will be both co-spatial and co-temporal with the 6 mHz signal, appearing as the signal overlaps.

3.2. Detection results

All the seismic sources detected in this active region during the time of the flare using the simple 5σ rule of the acoustic holography method are shown on the HMI magnetogram in Fig. 4 (left plot). The egression contours in 3-7 mHz frequencies for those four seismic sources clearly confirmed by the further statistical analysis (see sections 3.1.2 and 3.1.3) are shown on the HMI white light image in Fig. 4 (right plot). The point locations of the four seismic sources are indicated by the asterisks in the HMI white light image in Fig. 5 (left plot), where the future time–distance diagrams are obtained, while the sectors in the three seismic sources with the most significant statistical signals derived using the directional holography (see section 3.1.3) are shown in Fig. 5 (right plot).

The locations of these four acoustic sources coincide with some of the footpoints of the magnetic ropes formed just prior to the X9.3 flare onset as demonstrated by the simulations of (Inoue et al. 2018) and shown in Fig. 1. Namely, the acoustic source 1 (seen in holography and TD diagram) occurring during flaring event 1 is likely linked to the F3 footpoint in the northern end of the green rope (see Fig. 1). The strongest seis-

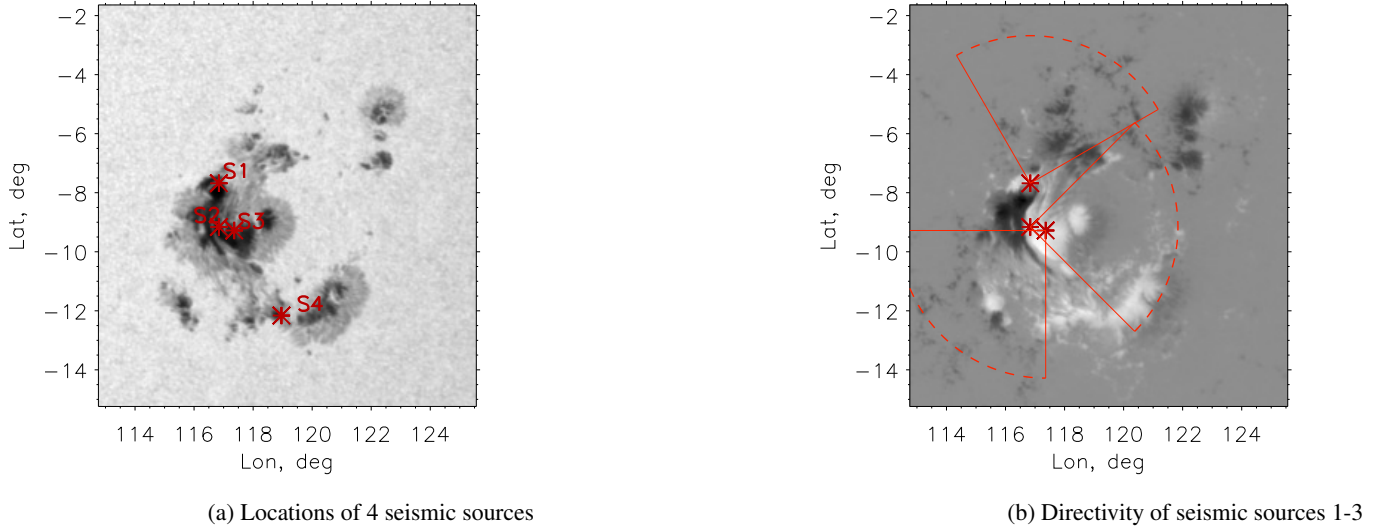


Fig. 5. (a) HMI white light image of the active region marked with the egression maps of the seismic sources 1-4; (b) Directivity maps of seismic sources 1-3 derived with directional holography shown by the sectors with detectable acoustic signals marked by the solid and dashed red lines.

mic source, source 2, which is clearly seen in holography and TD diagram, is linked to the F5 footpoint at the southern end of the green rope. Seismic source 3 (seen in holography and TD diagram) is linked to the F5 footpoint of the northern end of the blue rope and source 4 (seen only on holography) is linked to the F6 footpoint of the southern end of the blue rope.

Seismic source 4 was observed during the flaring event 2 during the second burst seen in GOES, RHESSI, and Ly- α line emission (see Fig. 2, middle and bottom plots). However, there was no significant HXR emission detected from the RHESSI image reconstruction in this location. Although, there was some belated HXR emission at the location of seismic source 2 during flaring event 2, as shown in Fig. 9, which helped us to guide the parameters of the beam heating this atmosphere. The presence of HXR emission shortly after the onset of FE2 indicates that there was likely another atmosphere heating with a shock leading to seismic source 5, which appeared 11 minutes after flaring event 1 at the location of seismic source 2. This assumption is also confirmed by the H α -line observations with detection of H α kernel 3 (see sections 4.2.1 and 4.2.2).

3.2.1. Detection with holography

Due to the temporal smearing intrinsic to the helioseismic egression measured using finite frequency bypass (Donea & Lindsey 2005; Macrae et al. 2018), the egression source appears much earlier and fades much later than the seismic ripples on the solar surface detected from TD diagrams (see the egression images in Fig.4). As described in 3.1.3, the choice of bandwidth leads to temporal smearing, and therefore it is not straight forward to extract accurate timings from the egression measurements alone, meaning that one can only detect the peaks within the flare time window. This explains the extra seismic sources detected with the simple 5σ method shown in

Fig.4a. The TD diagrams in this case provide a more reliable quake onset time due to avoidance of the temporal filtering, which prevents the 1000 s time smearing. In Fig.4b we show the example of egression contours in 3-6 mHz for the seismic sources 1 - 4, which demonstrates a difference in spectral appearances of different seismic sources; sunquakes 2 and 3 show the most pronounced signatures in all the frequencies, indicating greater depths of energy deposition into the solar interior, and SQ4 shows only the 6 mHz contour signalling a rather shallow depth for this deposition.

Figure 5a shows the locations of four seismic sources detected by us with the holography and TD diagram methods, which are similar to those reported by Sharykin & Kosovichev (2018) who used the former method only. In addition, in Fig.5b we show the directional diagrams of the acoustic signal propagation in the four holographic acoustic sources (1-4) detected in this flare. The locations of these four acoustic sources coincide with some of the footpoints of the magnetic ropes formed just prior to the X9.3 flare onset as demonstrated by the simulations of (Inoue et al. 2018) and shown in Fig. 1a. The acoustic source 1 occurring during flaring event 1 is likely linked to the F3 footpoint and has a directivity consistent with an angle of the shock deposition of $-(0 - 10)^\circ$. The middle (and strongest) acoustic source 2 clearly seen also during flaring event 1 is linked to the F4 footpoint and its directivity indicates an angle of -30° for the shock deposition.

Acoustic source 3, linked to footpoint F5 of the blue rope, has a directivity that is in agreement with an angle of $+30^\circ$ to the local vertical. Source 3 is likely to be the "source 4" detected by Sharykin & Kosovichev (2018) which is slightly east of the source 2 presented here. The most southern acoustic source 4 on the other hand is linked to footpoint F6 of the blue rope with an angle of the shock deposition of $+30^\circ$. This seismic source 4 was observed during flaring event 2

when RHESSI was observing, and during the second burst seen in GOES and Ly- α line emission (see Fig.2a and Fig.2b). However, there was no significant HXR emission detected from the RHESSI image reconstruction in this location (Fig.2c).

3.2.2. Detection with the time–distance diagram

The time–distance diagrams are detected in three seismic sources, or sunquakes (SQs): 1, 2 and 3. These TD diagrams are significant improvements on the seismic results reported earlier (Sharykin & Kosovichev 2018; Zhao & Chen 2018), since the TD diagrams for sources 1 and 3 are reported for the first time. Also, for the source 2 we were able to detect for the first time a second bounce of the acoustic waves produced in the flaring atmosphere of footpoint F4 discussed in the last few paragraphs of this section, which was predicted earlier (Duvall et al. 1997) but never observed in flares. Nevertheless, it was not possible to detect ripples with a TD diagram for seismic source 4. We suspect this is because the seismic source 4 was rather weak, only being seen by the holography method at the frequency of 6 mHz, which indicates that the heights of its ripples were at the level of the background noise, making them undetectable with a TD diagram.

The TD diagrams detected for SQ1-SQ3 are presented for seismic source 1 in Fig. 6 and for seismic source 3 in Fig.7. The most northern acoustic source, source 1, is located in footpoint F3 of the green loop, and seismic source 3 is located in footpoint F5. Their TD diagrams are computed from the surface signal centred on a field of view (FOV) of $284'' \times 129''$, as determined through directional egression analysis, over the 90° arc originating at 60° . In order to enhance the visibility of the surface wavefront, the surface remapping is carried out on a running difference of four Dopplergram frames (three-minute time difference). The resultant time–distance array is then thresholded to account for the perturbations at the flare location where the surface seismic ripples are observed as a ridge on the TD diagram.

As shown in Fig. 6 (*left*), the TD diagram of seismic source 1 shows a rather weak TD ridge, which becomes visible 15 minutes into the selected time range (starting at 11:55:37 UT). This ridge is highlighted in Fig. 6 (*right*) with an overplotted theoretical ray path. Manual fitting of the ray path to the signal ridge indicates an onset time for the quake of +7.5 minutes, resulting in the start time at 11:55:37 UT for the sunquake 1 (source 1 in flaring event 1). This is in agreement with the time of the observable LOS magnetogram transient peak, as well as the WL emission peak and is about 20s after the HXR emission onset (see the light curves; Fig. 2, top plot). The TD diagram shows that the ridge approached the end of the datacube of 120Mm with a velocity of 48 km/s. The TD diagram of seismic source 3 (Fig. 7, *left*) shows the ripples started at the same time as in the seismic source 1. Although, seismic source 3 has a deeper ridge (Fig. 7, *right*), which approaches the 120 Mm distance slightly quicker than in source 1, travelling with a velocity of 51 km/s.

The TD diagram for acoustic source 2, which is located in the F4 footpoint of the green loop, is computed from the

surface signal centred on $284'' \times 129''$, as determined through directional egression analysis (see Fig. 8), over a 90° arc starting at 60° . The results for seismic source 2 are presented in Fig.8 (*left*), where one can see the very deep TD ridge approaching a velocity of about 52 km/s at the edge of the data cube of 120 Mm, which become visible 8-10 minutes into the selected time range (starting with 0 minutes at 11:55:37 UT). This ridge is highlighted in Fig.8 (*right*) with an overplotted theoretical ray path. Manual fitting of the ray path to the signal ridge Fig.8 (*right*) indicates, similar to source 1, the onset time for the quake of +7.5 minutes, giving the sunquake start time at 11:55:37 UT (source 2 in flaring event 1). This is in agreement with the time of the observable LOS magnetogram transient peak, as well as the WL emission peak and about 20s later than HXR emission onset (see the light curves, Fig. 2, top plot).

There is also some indication of a unique feature seen for the first time on the time–distance diagram obtained for seismic source 2: a second ridge above the first one marked by the second white line in Fig.8. This second ridge indicates a second bounce from the surface of the acoustic waves (Duvall et al. 1997) propagating in the solar interior after their first bounce and reflection back to the surface by the interior because of Fermat principle. We believe these secondary directed ripples are those from the second bounce derived from HMI dopplergrams propagating in the directions shown in the holographic image (Fig. 5). The second ridge shown in Fig.8 has, as expected, a slower speed of the ripple propagation on the solar surface approaching about 27 km/s at the distance of 120 Mm. The second bounce acoustic waves are assumed to exist but until now have never been observed in this or any other flares. Examples of the first and second bounce acoustic waves can be also seen in the supplementary movie of the acoustic wave model provided in Paper 2 (Zharkova et al. 2020).

Here we wish to reiterate the fact that ridges on TD diagrams reflect the ripples coming from the centre of the flaring point (sunquake 2 in this case) where the shock is deposited and generates a set of acoustic waves of different frequencies (in mHz), which are the pressure waves propagating in the solar interior. These waves become reflected from hotter regions of the solar interior in accordance with the Fermat principle (Zharkov 2013) and become seen when the acoustic waves travel back to the surface, or the photosphere, and become reflected from it, producing a splash or ripple with a height of about 3 km above the surface (Kosovichev and Zharkova, 1998). This reflection of acoustic waves produces ripples of the first bounce, which appear to run away from the central location where the shock was deposited. Because acoustic waves are generated as sets of acoustic waves with different frequencies, each subsequent wave propagates into deeper interior and produces ripples of its first bounce further and further from the central location. Since these acoustic waves are coming from increasing depths in the solar interior, their reflections appear as ripples moving with increasing speed further and further from the point where the waves were generated by the shock. If one measures the time and distance from the shock location to the locations where the ripples occur, this appears as a ridge on the time–distance diagram.

We believe that in the interior beneath sunquake 2, the acoustic waves are reflected once from the photosphere in the first upper turning points, travel back to the solar interior, and become reflected from the inner layers of the solar interior at the bottom turning point in accordance with the Fermat principle (Zharkov 2013). These waves then travel back to the surface where they become reflected from the photosphere for the second time at the second upper turning points where the waves are reflected back to the solar interior. Therefore, the second bounce reflects the occurrence of secondary ripples appearing later after the first bounce and travelling slower in the interior because the waves were attenuated by travelling in the interior and reflection in the first bounce. Furthermore, because the acoustic waves continue to lose their energy in the solar interior, when they are reflected a second time, they produce smaller splashes with smaller heights above the photosphere than the first one. The occurrence of the primary and secondary ripples is shown in the online video associated with Paper 2.

We verified that there are no random sources present in the locations of source 2. Again, if there were another source of acoustic waves, its location would be offset from source 2 and thus would not be observed in TD diagrams centred on this source. While these two ridges are observed only in the few pixels around source 2, they are organised as circular ripples and are unlikely to have been produced by anything else but the shock. Therefore, these are likely to be the first and second bounces of acoustic waves in SQ2.

These second bounce ripples could also lead to resonant interference with the waves from the first bounce of seismic source 2 and with the waves of the repeated seismic source 5. The resulting waves could produce ripples with much greater bounce heights than the usual 3 km (Kosovichev & Zharkova 1998), approaching the chromosphere. These could be seen as ripples in Ca II spectrograms occurring in the chromosphere reported for this flare by Quinn et al. (2019) in SST data as was suggested for the similar observations of ripples in Ca II emission by Hinode (Kosovichev 2011).

4. Extreme ultra-violet and optical observations

4.1. Extreme ultra-violet signatures

The X9.3 flare was also observed with the EUV Imaging Spectrometer (EIS) aboard the Hinode spacecraft (Culhane et al. 2007), which is a scanning slit spectrometer that provides spectral information in a range of EUV lines in the wavelength ranges 170–210 Å and 250–290 Å, with a spectral resolution of $0.0223 \text{ Å pixel}^{-1}$. As part of a major flare watching campaign, EIS observed AR 12673 for some hours before and after the flare onset, catching the flare in its entirety. The HXR emission contours in flaring event 2 are over-plotted on the AIA He II 304 image (taken before the AIA emission became over-exposed) at 50, 70, and 90% of the peak intensity in Fig. 9, which is co-aligned with the EIS FOV overplotted as a white square. Also overplotted are black 6 mHz egression contours and cyan 30–60 keV HXR sources (from flaring event 2). The white vertical lines indicate the EIS slit positions that correspond to the locations of the egression contours. The EIS data

were corrected for dark current, hot pixels, and cosmic-ray hits using the standard calibration routines. Wavelength corrections were also applied to account for the temperature dependent variation of line position over the Hinode orbit and for the slit tilt. The duration of each raster was approximately 3 minutes.

The raster included ten wavelength windows, but we focus here on the He II 256.3 Å (radiative temperature of about $(8 - 12) \cdot 10^4 \text{ K}$) and Fe XXIII 263.76 Å (radiative temperature about $2 \cdot 10^7 \text{ K}$) lines that sample the response of the transition region (He) and the hot corona (Fe) to the flare energy release, respectively. As the EIS scans make an image, each slit position in the x direction not only represents a different spatial location but also a different time, while all y positions along the slit are simultaneous in time. While this selection limits the overall temporal resolution, it allows us to identify those slit positions during the raster that are spatially and temporally coincident with the sunquake (SQ) emission, and to compare the spectral response at those locations with the spectral response at other locations along the slit that are not associated with acoustic emission. The slit locations of interest are indicated in Fig.9 by vertical white lines.

In Fig.10 and Fig.11 we plot a series of He II 256.3 Å spectrograms at the slit positions that include the sunquake locations as well as a few slits to the east and west of those locations for comparison. The slit positions that correspond to strongest 6 mHz seismic sources are located at heliocentric locations at 528–540 arcseconds. The spectrograms illustrate the intensity of the emission as a function of heliocentric location on the y-axis and Doppler velocity (wavelength) on the x-axis. The wavelength axis was converted to velocity units using a rest wavelength derived from a pre-flare raster at 11:48 UT and the instrument spectral dispersion. Negative velocities indicate blueshifted or upflowing plasma, while positive velocities indicate redshifted or downflowing plasma. The black horizontal lines indicate the heliocentric location of the egression sources on the disc (N-S).

The upward macro-motions, seen as blueshifts, reflect chromospheric evaporation of the ambient plasma into the corona, while downward motion, seen as redshifts of the lines, including $H\alpha$, reflects hydrodynamic shocks moving towards the photosphere and beneath (Somov et al. 1981; Fisher et al. 1985a,b; Zharkova & Zharkov 2007; Zharkova & Zharkov 2015; Druett et al. 2017; Druett & Zharkova 2018). In paper 2 (Zharkova et al. 2020) we present flaring atmosphere models calculated as hydrodynamic responses to the injections of particle beams which we use to interpret these macromotions. From these simulations it is evident that these macromotions are associated with the same flaring atmospheres, thus closely linking the locations of blueshifts and redshifts. We also demonstrate in paper 2 (Zharkova et al. 2020) that the sunquakes detected for this flare are generated by the same hydrodynamic shocks propagating with supersonic speeds in the solar interior beneath flaring atmospheres where particle beams are injected.

It can be seen from Figs.10 and 11 that there is emission in the line along the length of the slit, and that in many cases the emitting plasma is at rest, or is not redshifted (0 km/s), because the line profiles are symmetric and centred about the central wavelength. However, in the few locations associated with the

egression source locations (black lines) He II emission profiles with redshifts can be clearly identified in the three bottom rows between (-250", -220") as both are more intense and elongated in the positive x-direction. This elongation indicates downward Doppler motions of the flaring plasma leading to an asymmetric intensity distribution skewed towards the red wing.

In this case it can be observed that there are asymmetries associated with the egression source locations (black lines) both to positive and negative velocities of several hundred kilometres per second. The most intense He II emission appears shifted towards positive velocities (redshift; the bottom three rows for flaring atmospheres with SQs 1-3, indicating the downflows of >250-300 km/s caused by hydrodynamic shocks generated in these atmospheres). These shifts appear at the start of flaring event 1 (and sunquakes (SQs) 1-3) and last for 90 seconds before the appearance of blueshifted profiles during the flare relaxation phase (shown in the upper four rows when downward moving material returns back to the solar atmosphere from the interior, thus showing upflows, or lines with blueshifts).

In Fig.10 we show these downflows and upflows in more detail by plotting the He II line profiles for six slit positions in time shown on the top of each window. The SQ locations associated with these motions are indicated at the slit positions with a black line. These include the locations of the egression sources, as well as the positions within the flare ribbons outside of the egression sources. The X positions are plotted on the left-hand side of each spectrum: 528" (the left column), 536" (the central column) and 540" (the right column). The observation time starts from the time close to the SQ onsets (the right-most plot) and continues to later times from right to left. These locations correspond to the locations of SQs 1, 2, and 3. As can be seen from the He II profiles, the emission is predominantly redshifted in the SQ locations. Given the complex nature of some of the line profiles, we do not fit the lines (e.g. slit position 536"), but use the rest wavelength and spectral dispersion to indicate the range of velocities present.

Contrary to the redshifts shown at the start of flaring event 1 in He II line profiles in Fig. 11, the Fe XXIII line profiles shown in Fig.12 demonstrate from the very start the increasing blue asymmetry of the Fe XXIII line at several locations along the slits that sample SQs 1, 2, and 3 (bottom three rows of the plots). The blueshifts are highest at the onset of flaring event 1 in source 2 and are slightly lower in SQ 1 and 3.

Figure 13 displays the spectrograms of the Fe XXIII 263.76 Å line for flaring event 1, where one can see predominantly blueshifted velocities of several hundred kilometres per second with upflows in excess of 300-400 km s⁻¹ observed around (528-532", -232-243"). In this case, the velocity scale was derived relative to the laboratory rest wavelength as Fe XXIII is only produced in plasmas of T>10MK during flare conditions, so that no 'quiet' sun reference is available. In both He II and Fe XXIII spectrograms, it is clear that large asymmetries and flows are observed at flare onset, as expected. Unfortunately, the EIS FOV does not include a location of the seismic source 4. However, the He II line response showing redshifts of > 150 km/s was detected in the location of the possible repeat sunquake 5 (not shown here), which occurred during the flaring

event 2 in the same location as the seismic source 2 and H α kernel 3.

4.2. Hydrogen H α line and white light emission

4.2.1. Images of H α -sources with redshifts

We used the H- α observations by the CRISP Imaging Spectro-Polarimeter (CRISP) (Scharmer et al. 2003; Scharmer 2006) at Swedish Solar Telescope (SST), which is equipped with three high-speed, low-noise CCD cameras that operate at a frame rate of 36 fps, making it an adept instrument for spectroscopic imaging of the H α line (6562.8 \pm 1.5 Å). The H α line observation sequence occurred from 11:55:50 UT to 12:51:58 UT, which captured the X9.3 class flare within the 55 \times 55" CRISP FOV (see Figs.14, top panels) with a cadence of 15 seconds. The reduction and processing of this data was carried out by the group at the Queens University Belfast (Quinn et al. 2019) using the general procedures for the reduction of CRISP data (see their methods section in Druett et al. 2017).

For the H α line observations, we focus on the CRISP frames with the timings pertinent to the evolution of the sunquakes. We identify two locations for the study of the H α line profiles using frame 0. The next three images in the sequence have very poor seeing conditions, and the SST field of view is adjusted between two of those frames. Additionally, the flare ribbons evolve rapidly over the one-minute period between clear images, making it impossible to track the changes in the small flaring kernels 1 and 2 during that period.

The identified kernels are: Kernel 1, which is closely co-spatial with the seismic source 1, possibly indicating the northern footpoint F3 of the green magnetic rope (see Fig.1), which later erupted during flaring event 1; the second kernel (kernel 2) was located close to the northern footpoint F5 of the blue magnetic rope, which produced seismic source 3 (see Fig. 1, left); H α kernel 3 was observed at 12:06:48 UT during flaring event 2 at the location of the southern footpoint F2 of the red rope. This footpoint was close to the location of footpoint F4 of the green rope (Fig. 1, right), which erupted before flaring event 2 freeing the space for the footpoint F2 of red rope. Its location is close to seismic source 2 but the event likely occurred 10 minutes later as a new seismic source 5. As a result of the overlap with the seismic signatures produced by the largest seismic source 2 and source 3 in this particular location, we cannot distinguish the individual properties of source 5. Unfortunately, there is no H α line observation for the location of the seismic source 4, which appeared at 12:06:48 UT, because it was outside of the CRISP field of view.

The top panel of Fig.14 shows the images taken at 11:55:50 UT (left) and 12:06:48 UT (right) in H α (6563 + 1.5) red wing emission. Kernel 1 (red circle) occupied five pixels in the observation at 11:55:50 UT, representing an area of around 9245 km² (equivalent area to a 96 by 96 km box). This frame is of particularly good image quality and shows enhanced red wing emission in the northern end of the eastern ribbon, as highlighted by the red circles in Fig.14 in H α kernel 1. The line profile in each kernel was produced by taking the average of the profiles from these five pixels, which were individually alike.

The average profile for kernel 2 (blue circle) was produced in a similar way, by taking the average of the similar profiles over 14 pixels, covering an area of around 25,900 km², equivalent to the area covered by a 161 by 161 km box. The emission in kernel 2 shows an enhancement in the red wing at 11:55.50 UT; it is shown in the location marked by a blue circle, where the seismic source 2 was located.

The H α emission in kernel 3, whose location is indicated by the green circle in Fig. 14, shows enhancement in the red wing of the H α line profile occurring 1 minute before the RHESSI HXR signatures detected after about 12:08:26 UT (see Fig. 14, top right plot). This emission occupies 22 pixels showing similar profiles over an area of 40,680 km². The HXR emission contours in flaring event 2 are over-plotted at 25, 50, 70, and 90% of the peak intensity on the H α image in Fig. 14. We note the difference in HXR contours shown on top of the EIS image (see Fig. 9, cyan contours) and the H α image here in Fig. 14; their different views are related to the different spatial resolutions of the EIS (4''), RHESSI (2''), and SST (0.06''). Evidently, on the EIS image the HXR contours appear small while on the H α image the HXR contours are larger.

During FE1, the H α -ribbons grow and expand away from each other showing weak signs of wave propagation, similar to those reported for the Ca II line (Quinn et al. 2019). There are strong red wing asymmetries observed at the ‘leading edges’ of the expanding H α ribbons (i.e. the leading edge of the ribbons as they expand outwards and separate). The profiles in a fixed location are initially placed at the leading edge of the expanding ribbon; they start off with a strong asymmetry and become more centrally enhanced and symmetric as the ribbon expands, moving into the locations in internal parts of the ribbon. As the flare enters its latter stages following the impulsive stage, the H α line profiles become narrower.

4.2.2. H α -line profiles

The H α profile of the spectral data from the H α kernel 1 is shown in Fig. 14 (bottom panel, red line). This feature does not have strong emission in the H α line core. However, it does have highly enhanced red wing emission, with the emission intensities still increasing as one moves up to 1.5 Å from the line centre (see Fig. 14). The H α line profile in kernel 2 (the blue line in the bottom panel of Fig. 14) is also likely to show the emission profile with strong red asymmetry catching only the intensity of a blue wing, with the central part of the profile being strongly redshifted beyond the available CRISP spectral window of 3 Å. Therefore, it is certainly possible that the core profile intensities in both H α kernels 1 and 2 will be shifted well above 3-4 Å in the red wing for both these kernels, thereby falling outside the observed wavelength range of the spectral window. This assumption can be only tested by the simulations presented in paper 2 (Zharkova et al. 2020).

The profile in H α kernel 3 (green line, right panel) for flaring event 2 at 12:06:48 UT shows a much larger intensity rise in the near blue wing than in flaring event 1 (kernel 1), indicating a redshift larger than the size of the spectral window (>3 Å). This is similar to the behaviour seen in H α kernel 2, which co-

incides with seismic source 2. Hence, it can be also argued that we only observe a blue wing of the H α emission, and see little sign of the central core emission with self-absorption, as this part of the line is shifted to the red wing outside the spectral window of CRISP.

The H α line profiles observed in kernels 1 to 3 are strongly reminiscent of the central sections of the profiles from, for example, Ichimoto & Kurokawa (1984), which show very large redshifts (see their Fig. 3a, profile at 00:19:59 UT or their Fig. 4a, profiles from 06:44:20 UT and 06:44:28 UT with emission profiles peaking 2 to 5 Å from the line centre). These unusual H α line profiles highlight the challenges in analysing the chromospheric dynamics of strong flares obtained with modern instruments that have H α spectral windows extending to less than ± 1.5 Å from the line centre used in SST.

These unusual H α line profiles closely resemble those simulated for flaring atmospheres heated by strong beams (Druett & Zharkova 2018) and their interpretation will be provided in paper 2 (Zharkova et al. 2020).

4.3. White light emission

In the continuum images observed by SDO/HMI, AR NOAA 12673 appears to be made up of a main delta spot (S1) surrounded by some smaller spots (S2-S5) in the northern and southern parts of the active flaring events (top panel of Fig. 15). The WL emission of the X9.3 flare is relatively intense and exhibits a clear ribbon shape, including the same regions previously involved in the first X2.2 flare (Romano et al. 2018). The area covered by the WL ribbons in the continuum filtergram at 11:59 UT reaches a maximum extension of about 9.2×10^7 km².

We selected two cases of the enhancements in white light emission in the HMI continuum during the flaring events of the X9.3 flare shown in Fig. 15 during the flaring event at 11:55:56 UT located in H α kernel 2 (left plot) and 12:06:00 UT located in H α kernel 3 (right plot). The pixels from the first WL event were located in seismic source 2 and those from the second WL event were located in seismic source 4. It can be observed that WL emission in both events grows very sharply at their beginning. However, the emission in WL event 1 occurred during FE1 drops very sharply after its maximum, while WL emission in the second WL event occurred during FE2 has double peaks and shows much slower decay over time, indicating larger initial intensity of the hydrogen continuous emission in Paschen continuum as was proposed by Druett & Zharkova (2018). In Paper 2 (Zharkova et al. 2020) we will present the simulated light curves of hydrogen Paschen continua for these two kernels associated with white light emission and H α kernels.

5. Possible plasma parameters of flaring events in sunquake locations

5.1. Input from high-energy emission

In this paper we explore the physical conditions linked to the formation of multiple seismic sources during the 6 September 2017 X9.3 flare by comparing parameters derived from helio-

seismic and spectral observations in EUV and optical emission with those derived from radiative hydrodynamic models of flaring atmospheres and hydrodynamic models for acoustic wave formation in the solar interior. X9.3 flare occurred in NOAA AR 12673 and had four flaring events, from which we investigated two: flaring event 1 at 11:55:37 UT observed in GR, HXR with KONUS instrument aboard WIND satellite, EUV emission with EIS, WL and dopplergrams with HMI, $H\alpha$ emission with SST and flaring event 2 at 12:06:40 UT observed by SST and partially by RHESSI (Lin et al. 2002). Both events were also recorded with $Ly\alpha$ light curves observed by LYRA instrument onboard the PROBA 2 satellite. The magnetic structure in this AR was revealed by NLFFF extrapolation of magnetic field after the previous X8.2 flare occurred 2 hours before X9.3 flare while the 3D MHD simulations revealed the evolution of the magnetic structured leading to a formation just prior to the X9.3 flare onset of three magnetic flux ropes (MFRs) (Inoue et al. 2018). The places where these MFRs were embedded into the photosphere are considered to be the locations of the four (possibly five) sunquakes detected during the X9.3 flare.

The multi-channel spectral observations by the KONUS instrument of flaring event 1 in 200 keV - 15 MeV energy range during the main flare peak demonstrate the existence of powerful mixed particle beams with electron and proton components. The proton spectral index in the ≤ 30 MeV energy range is estimated to be about 4 (Lysenko et al. 2019). We obtained averaged HXR energy spectrum derived from the KONUS instrument, from we derive an averaged spectral index of the particle spectrum of 4, and a total energy flux of $1.1 \cdot 10^{31}$ erg (Lysenko et al. 2019). Moreover, in the discussion of their paper, Lysenko et al. (2019) report that during the initial impulsive phase the lower energy part of the HXR spectrum revealed a soft-hard-soft (SHS) pattern indicating that the beam which heats flaring atmospheres in this event had to have a large initial energy flux increasing and decreasing in time as a triangle function. It has been shown from the kinetic Fokker-Planck solutions (Zharkova & Gordovskyy 2006) that the SHS pattern in the HXR energy spectrum indicates the presence of strong return currents formed by lower energy electrons of the beam moving back to the source, if the beam energy flux becomes much higher than $5 \cdot 10^{11}$ erg \cdot cm $^{-2}$ s $^{-1}$.

Since the KONUS data do not have any spatial resolution, while we observed locations on the surface of three seismic sources, EUV emission sources, three $H\alpha$ kernels and two WL kernels with different spatial resolution, we need to use the areas of $H\alpha$ line kernels in the locations of sunquakes (SQ) 1 - 3 to evaluate the total area where the energetic particles were injected. This approach will allow us to derive the initial energy fluxes in each SQ location. By measuring the areas in two $H\alpha$ kernels 1 and 2 and assuming that the area of SQ3 is similar to the average between SQ1 and SQ2, we estimate their total areas to be close to $2 \cdot 10^{15}$ cm $^{-2}$. Considering the duration of the FE1 to be about 500s, we can determine the energy parameters of particle beams to be about 10^{13} erg \cdot cm $^{-2}$ s $^{-1}$, which can vary by a few units and still be of the same order of magnitude in each of the three SQs. Based on the $H\alpha$ line profiles and their occurrence simultaneously with HXR emission, we have to assume that there were very energetic electrons in the mixed

beams injected into the footpoints where seismic sources 1 and 2, and possibly 3, occurred. However, because SQ in seismic source 2 was the strongest one, we have to assume that the mixed beam in this SQ was the strongest. In Paper 2, the exact coefficients for the initial energy flux in each SQ will be tuned after fitting theoretical $H\alpha$ line profiles to those observed during this flare (Zharkova et al. 2020).

Based on the observations of strong hard X-ray emission in the flaring event associated with the sunquake, we assume that flare emission is produced by injection of subrelativistic electron beams with power-law energy distributions (Brown 1971; Syrovatskii & Shmeleva 1972) into the chromosphere of the quiet Sun (QS) from the primary energy release point in the corona. The beam electrons are assumed to heat the cold ambient chromospheric plasma, sweeping it like a piston to deeper atmospheric levels (Syrovatskii & Shmeleva 1972). This heating prompts a hydrodynamic response of the ambient plasma, turning the QS chromosphere into a flaring atmosphere (Somov et al. 1981; Zharkova & Zharkov 2007). The simulation of a hydrodynamic response provides column depth distributions of the kinetic temperature, density, and macrovelocities of the ambient plasma for different instances after the beam onset.

5.2. Parameters of seismic sources

There were four seismic sources detected in this flare with the directional holography of the acoustic signal propagation. Their locations coincide with the footpoints of the magnetic flux ropes formed just prior to the flare X9.3 onset derived from the NLFFF and MHD simulations (Inoue et al. 2018). The most northern seismic source, source 1, is likely linked to the northern end of the green rope, seismic source 2 is likely linked to the southern end of the green rope, and seismic source 3 is likely linked to the northern end of the blue rope. Seismic source 4 was observed in the southern part of this active region, possibly in the southern footpoint of the blue rope.

The three seismic sources 1-3 were also detected with the TD diagrams, with the most powerful seismic source 2 revealing, for the first time, first and second bounces of acoustic waves. The TD diagram of source 1 reveals the start of ridge 20 minutes after 11:55:37 UT at the distance of 20-25 Mm from the location of shock deposition, while the source 3 ridge appears at about 6 minutes at a distance of 10 Mm. The phase velocities of ripple propagation on the surface approach 48 km/s (source 1) and 51 km/s (source 3). The TD diagram of source 2 shows a very sharp ridge with the initial phase velocity of $35 - 40$ km \cdot s $^{-1}$ approaching 53 km \cdot s $^{-1}$ at the edge of the 120 Mm data cube. The first bounce, or upper turning point, for source 2 occurred at 5 - 8 Mm where the first bounce ripples are detected.

There were also ripples of the second bounce detected in source 2 propagating with a velocity of 27 km/s at 120 Mm. Because of the observation of the $H\alpha$ line profile of kernel 3 with a large redshift detected in the same location as source 2 but 11 minutes later, we can assume that there was a further acoustic source, source 5, during flaring event 2. The three seismic sources (2, 3, and 5) in close physical proximity can

cause resonant interaction of the acoustic waves generated in these sources. As a result, the amplitudes of the ripples generated by the upper bounces of these acoustic waves can be significantly increased, allowing their observation in the chromospheric emission of the Ca II line, which was reported for this flare by Quinn et al. (2019), and resembles some earlier events in Ca II seen by Hinode payload (Kosovichev 2011).

5.3. Summary of the EUV observations

These two flaring and multiple seismic events were observed with the SDO/AIA and Hinode/EIS instruments in EUV emission. From the Hinode EIS observations of the Fe XXIII 263.76 Å line we detect dominant blueshifted velocities of several hundred kilometres per second in the locations of seismic sources 1 and 3 with upflows in excess of 300-400 km s⁻¹ at the locations of seismic source 2. In both He II and Fe XXIII, it is clear that the largest asymmetries and flows are observed at flare onset. The largest velocities are also observed by the EIS instrument at the flare onset, as defined by the rise of the 80 - 300 keV emission observed by KONUS-WIND (Fig.2), when both blueshifts and redshifts in EUV emission of several hundred kilometres per second are observed. Redshifts in excess of 200 km s⁻¹ were observed at locations that are well correlated with sunquakes 1 and 2 in the northern part of the active region.

In Fig.13 we display the spectrograms for the Fe XXIII 263.76 Å line for flaring event 1, which show large blueshifted velocities of the upflows of up to 400 km s⁻¹. This is combined with the average downflows of > 150-250 km s⁻¹ up to 300 km s⁻¹ seen in He II 256.32 Å at the location of SQs 1, 2, and 3. It is clear that the largest asymmetries and large flows are observed at the onset of each flaring event within the first 5-20 seconds, or during the injection of particle beams.

The magnitudes of macrovelocities observed for the He II 256 Å line for flaring event 1 approach 380 km/s as shown in the plots of Figs.10 and 11 (third bottom row). For the hotter line of Fe XXIII 263 Å the upwards velocity quickly (in the 10-15 sec) exceeds 400 km/s following the event onset, as shown in the plots of the bottom rows of Fig. 12, and in the three rightmost plots of Fig.13. Also, the redshifts of the downward motion measured in the He II line for sources 1 - 3 range between 150 and 300 km/s with the average magnitude being about 250 km/s as reported in Figs. 10 and 11.

5.4. Input from H α line observations

In the X9.3-class flare on 6 September 2017 there are two H α ribbons with very fine structure displaying complex behaviour over large areas similar to those reported by Druett & Zharkova (2018); the profiles will be described in more detail in the paper 2 (Zharkova et al. 2020). Nonetheless, we were able to detect two H α kernels (1 and 2) for flaring event 1 and one H α kernel (3) for flaring event 2 with noticeable H α line emission, from which we derived the line profiles shown in Fig. 14. The H α -line profile derived in kernel 1 coinciding with footpoint F3 is likely located at the northern end of the green magnetic rope (see Fig. 1, left). The H α -line observation in kernel 2 was

co-temporal with H α kernel 1 while located at footpoint F4 at the southern end of the green magnetic rope in the left panel of Fig. 1, coinciding with seismic source 2. There is no H α -line kernel detected for the location of seismic source 3, which has the most peculiar dynamics; these will be described in the paper 2 (Zharkova et al. 2020). The H α line emission in kernel 3 occurred about 10 min later than in kernels 1 and 2, during the flaring event 2, in the location of seismic source 2.

H α line observations were focused on the locations and timings pertinent to the evolution of sunquakes 1 - 3 in flaring event 1 and sunquake 5 in flaring event 2. This allowed us to detect two H α kernels (1 and 2) in flaring event 1 in the relevant locations of seismic sources 1 and 2, which show large redshifts in the H α line profiles. The H α kernel 3 was observed in the same location as seismic source 2 but during flaring event 2 allowing us to assume there should be the seismic source 5 in this location. The H α line profiles in kernels 1 and 2 were observed at 11:55:50 UT by taking an average of the profiles from all five pixels, where H α emission with the redshift was seen. These profiles reveal highly enhanced H α line emission with large redshifts, with the emission intensities still increasing at 1.5 Å from the line centre (see Fig.14, left column) restricted by the spectral window of the CRISP instrument (± 1.5 Å).

The average H α -line profile in kernel 2 associated with seismic source 2 does not show a strong H α intensity increase compared to H α kernel 1, suggesting a more distant blue wing of the H α line in kernel 2 compared to H α kernel 1 (showing a near blue wing). This difference in blue wing emission can be caused by a slightly larger redshift in the flaring atmosphere of kernel 2 than in kernel 1. In other words, the H α -line profile observed in kernel 1 has a higher intensity than in kernel 2, revealing a blue wing that is slightly closer to the line core than the one in kernel 2. Indeed, the H α line profile in kernel 2 is consistent with a very large redshift caused by a strong hydrodynamic shock travelling with velocities exceeding 300 km/s induced by a mixed beam (Zharkova et al. 2020). This also agrees with a reduced enhancement of the white light emission of the X9.3 flare in H α kernel 2 peaking at 11:55:56 UT (event 1) compared to the WL emission in H α kernel 3 seen in the flaring event 2 after 12:06:48 UT (event 2). For details of the interpretation of these profiles we refer to paper 2 (Zharkova et al. 2020).

We wish to emphasise that while the flare was observed by many instruments throughout its duration, there are disparities in coverage and in the spatial resolution of different instruments. As the KONUS observations do not have any spatial resolution and there were no RHESSI observations available during flaring event 1 after 11:55:37 UT when the sunquakes were observed and the first H α line profiles in kernels 1 and 2 are taken a few seconds later, a comparison of the observed and simulated H α -line profiles in these kernels had to be based on a simple visual agreement of the shape of the H α -line profiles and the current understanding of the effects of flare energy release on line formation. This latter information was gathered from both the observations explained in detail above and from modelling that will be explained with plots in Paper 2 (Zharkova et al. 2020).

Given that the area covered by $H\alpha$ emission in kernel 1, which occurred at the start of flaring event 1, we believe it is safe to suggest that it could be produced by beam electrons with an energy flux of about $(6 - 8) \cdot 10^{12} \text{ erg-cm}^{-2}\cdot\text{s}^{-1}$. We can still use a spectral index of 4 derived from the KONUS observations. While the $H\alpha$ line profile observed in kernel 2 has a lower intensity than in kernel 1, its area is smaller than that of kernel 1, indicating that the mixed beam should have a higher initial energy flux of $(8 - 12) \cdot 10^{12} \text{ erg-cm}^{-2}\cdot\text{s}^{-1}$ and the similar spectral index of 4 as in the $H\alpha$ kernel 1. Because of the small area of the $H\alpha$ kernel 3 and the absence of HXR emission at the start of flaring event 2, the initial energy flux of the beam that produced this emission remains unknown. However, only the blue wings of the $H\alpha$ line profile were observed without the line cores in kernels 1, 2, and 3, thus, indicating that the redshifts in these kernels were rather substantial. For an interpretation of these profiles we refer to Paper 2 (Zharkova et al. 2020).

6. Conclusions

Precise interpretation of these multi-wavelength observations of the flare is hampered by the differences in temporal coverage and spatial and temporal resolutions of the different instruments. The nature of the KONUS instrument is such that the spatial resolution information for gamma ray emission is unavailable. In addition, the spatial resolutions of HXR emission ($2''$), EIS observations ($4''$), and H-alpha line profile with SST ($0.06''$) are very different, meaning that one can only realistically provide some limits on the energy deposition throughout the atmospheres in each location. Modelling is required in order to make further progress in understanding these events, but it is hoped that these observations can provide important additional new constraints for the models. This modelling is the subject of paper 2 (Zharkova et al. 2020). Below we summarise our current findings.

In this study, similarly to other authors (Sharykin & Kosovichev 2018; Zhao & Chen 2018), we detected four seismic sources using the holography method. In addition, we derived three TD diagrams in these sources, adding a further two TD diagrams for seismic sources 1 and 3. Also, for source 2, we report the detection of not only one but two bounces of the acoustic waves produced in the flaring atmosphere in footpoint F4; the second bounce was theoretically predicted (Duvall et al. 1997) but had never been previously observed in flares.

Sunquakes 1 and 3, appearing temporally close to sunquake 2, are associated with footpoint F3 and F5, respectively. SQ1 has also the $H\alpha$ -line kernel 1 observed at the same location, while SQ3 did not have any. The initial beam energy fluxes in the footpoints F3, F4 and F5 were defined from the areas of the two $H\alpha$ line kernels in FE1 using the general parameters of HXR and γ -ray emission observed by KONUS at the onset of this flaring event 1. The beam deposition in each footpoint is assumed to generate a hydrodynamic response of flaring atmosphere leading to the formation of low temperature hydrodynamic shock moving with large velocity towards photosphere and solar interior. We establish the angle of deposition of the shock-generated sunquake 1 towards the photosphere vertical to be about $-0 - 10^\circ$ according to the directional holography

approach, while for the sunquake 3 the shock was deposited under the angle of $+30^\circ$ from the local vertical to the surface. We also measured the upflowing motion of hot plasma in flaring coronas well above 200 km/s appearing in both SQ1 and SQ3 up in the very first seconds of the event onset. Being restricted by the spectral window of the CRISP/SST instrument of $\pm 1.5 \text{ \AA}$, the observed $H\alpha$ line profile in kernel 1 had rather unusual shape increasing with wavelength and without a line core. This profile indicates a possibility that we observe a blue wing of the $H\alpha$ line profile caused by the shock whose macrovelocity exceeding 200 km/s, thus, shifting the line core to the red wing by more than 3-4 \AA .

For seismic source 2 occurring in footpoint F4, seen also in EUV emission with the upflowing velocities up to 400 km/s, WL kernel and in the $H\alpha$ emission in kernel 2, the $H\alpha$ line profile observed with the spectral window of $\pm 1.5 \text{ \AA}$, by the CRISP/SST instrument has the similar shape as in kernel 1. Although, it has much lower intensity of the blue wing than in $H\alpha$ kernel 1, e.g. pointing out to the much further blue wing of the $H\alpha$ line profile which has a lower intensity than in kernel 1. This indicates that the redshift in kernel 2 was caused by the shock with much higher macrovelocities (above 250 km/s) than in kernel 1. This shock must be rather strong (with much higher velocity of the shock) because it has to be capable of producing the strong sunquake 2 with acoustic waves showing not only single but a double bounce. The angle from the local vertical of the shock deposition in the flaring atmosphere for SQ2 in footpoint F4 derived from the directional holography is $\approx 30^\circ$.

Again, the parameters of the agents delivering energy from the top to the lower atmosphere and forming the shock that generates sunquake 2 in FE1 have to be in the agreement with those derived from the KONUS HXR data. During FE1 there were three seismic sources recorded, and, therefore, we can assume that HXR emission observed by the KONUS instrument came from all three sources and we can use the areas of $H\alpha$ kernels 1 and 2, and the area of seismic source 3 to derive the total area, from which this HXR emission was produced. This will allow us to evaluate the initial energy fluxes of the agents that will be done in Paper 2 (Zharkova et al. 2020).

These latter assumptions include the temporal variations of the HXR energy spectrum of the KONUS instrument following a soft-hard-soft pattern (SHS), which suggests a very high-initial energy flux of the injected beam at the peak of injection. Also we need to assume the temporal profile of the agent energy variations, e.g. assuming a triangular temporal profile of injection of very intense beam for a limited time. In addition, we have to account for a smaller increase in the $H\alpha$ line blue wing intensities at the location of kernel 2 (and seismic source 2) in comparison to $H\alpha$ kernel 1 (and seismic source 1). Since during flaring event 1 there were three seismic sources recorded, then we can assume that HXR emission observed by the KONUS instrument came from all three sources and, therefore, we can use the areas of $H\alpha$ kernels 1 and 2, and the area of seismic source 3, to derive the total area, from which this HXR emission was produced. The initial energy flux in each kernel is then defined by its respective areas. This leads us to the logical conclusion that the initial energy flux of injected beams in

atmospheres with $H\alpha$ kernels 1 (SQ1) and 2 (SQ2) should be of the order of $10^{13} \text{ erg} \cdot \text{cm}^{-2} \cdot \text{s}^{-1}$, being higher in kernel 2 than in kernel 1.

Unfortunately, during flaring event 2 the SST field of view was focused only on the northern and central part of the active region and, therefore, it missed any $H\alpha$ observations associated with seismic source 4. However, SST managed to observe the $H\alpha$ -kernel 3 occurring at 12:06:40 UT during FE2 in the location of SQ2, which was potentially associated with the undetected seismic source 5. Hard X-ray observations by RHESSI were made 1 minute later after the FE2 onset and can be only used for general guidance. These $H\alpha$ kernel 3 observations can only be linked with the white light observations in this location, which can be used for the evaluations of possible initial energy flux of the beam leading to appearance this $H\alpha$ kernel and WL emission. The observed $H\alpha$ line profile in kernel 3 is shown to be also strongly redshifted. From the shape of $H\alpha$ line profile in kernel 3 one can observe the blue wing emission similar to that seen in kernel 2.

Hence, in order to interpret the observed $H\alpha$ -line profile in kernel 3 (in the potential seismic source 5) in FE2, one needs to assume the atmosphere to be heated by a strong mixed beam with an initial energy flux of $(8 - 10) \cdot 10^{12} \text{ erg} \cdot \text{cm}^{-2} \cdot \text{s}^{-1}$ based on a large redshift in the $H\alpha$ line profile and blue wing emission similar to that in the $H\alpha$ kernels 1 and 2 observed in FE1. However, more quantitative verification of these suggestions are presented in paper 2 (Zharkova et al. 2020).

Based on the parameters of $H\alpha$ kernels and seismic events derived from the observations, in Paper 2 (Zharkova et al. 2020) we will consider two separate hydrodynamic models: 1) for flaring atmospheres heated by electron and/or proton beams, while producing hydrodynamic shocks deposited to the solar surface and into the solar interior, and 2) for generation of acoustic waves in the solar interior by these shocks and their reflection from the solar surface seen as sunquake ripples. These models are expected to provide some plausible insight into the seismic signatures of the sunquakes reported during this X9.3 flare.

Acknowledgements. The authors would like to thank the anonymous referee for constructive and helpful comments, from which the paper strongly benefited. The authors express their gratitude to Dr. A. Lysenko (IOFFE Institution, St. Petersburg, Russia) for offering the KONUS data with their full explanations and useful discussion. The authors acknowledge that HMI and AIA images are available by courtesy of NASA/SDO and the AIA, EVE, and HMI science teams. The Swedish 1-m Solar Telescope is operated on the island of La Palma by the Institute for Solar Physics of Stockholm University in the Spanish Observatorio del Roque de los Muchachos of the Instituto de Astrofísica de Canarias. LYRA is a project of the Centre Spatial de Liege, the Physikalisch-Meteorologisches Observatorium Davos, and the Royal Observatory of Belgium, funded by the Belgian Federal Science Policy Office (BELSPO) and by the Swiss Bundesamt fuer Bildung und Wissenschaft. S. Matthews acknowledges a financial support from STFC via the Consolidated Grant ST/N000722/1. S.Zharkov and V.Zharkova acknowledge the funding for this research provided by the U.S. Air Force grant PRJ02156. M.Druett's research is supported by the Swedish Research Council, grant number 2017-04099.

References

- Aboudarham, J. & Henoux, J. C. 1987, *A&A*, 174, 270
- Allred, J. C., Hawley, S. L., Abbett, W. P., & Carlsson, M. 2005, *ApJ*, 630, 573
- Antonucci, E., Gabriel, A. H., Acton, L. W., et al. 1982, *Sol. Phys.*, 78, 107
- Aptekar, R. L., Frederiks, D. D., Golenetskii, S. V., et al. 1995, *Space Sci. Rev.*, 71, 265
- Braun, D. & Lindsey, C. 2000, *Sol. Phys.*, 192, 307
- Brown, J. C. 1971, *Sol. Phys.*, 18, 489
- Buitrago-Casas, J., Martinez Oliveros, J., Lindsey, C., et al. 2015, *solphys*, 290, 3151
- Cally, P. S. 2006, *Philosophical Transactions of the Royal Society of London Series A*, 364, 333
- Canfield, R. C. & Gayley, K. G. 1987, *ApJ*, 322, 999
- Culhane, J. L., Harra, L. K., James, A. M., et al. 2007, *Sol. Phys.*, 243, 19
- Del Zanna, G. 2008, *A&A*, 481, L69
- Dominique, M., Hochedez, J.-F., Schmutz, W., et al. 2013, *Sol. Phys.*, 286, 21
- Dominique, M., Zhukov, A. N., Heinzel, P., et al. 2018, *ApJ*, 867, L24
- Donea, A. 2011, *Space Sci. Rev.*, 158, 451
- Donea, A. & Lindsey, C. 2005, *ApJ*, 630, 1168
- Donea, A.-C., Besliu-Ionescu, D., Cally, P. S., Lindsey, C., & Zharkova, V. V. 2006, *Solar Physics*, 239, 113
- Donea, A.-C., Braun, D. C., & Lindsey, C. 1999, *ApJ*, 513, L143
- Donea, A.-C., Lindsey, C., & Braun, D. C. 2000, *Sol. Phys.*, 192, 321
- Druett, M., Scullion, E., Zharkova, V., et al. 2017, *Nature Communications*, 8, 15905
- Druett, M. K. & Zharkova, V. V. 2018, *A&A*, 610, A68
- Druett, M. K. & Zharkova, V. V. 2019, *A&A*, 623, A20
- Duvall, T. L., Jr., Kosovichev, A. G., Scherrer, P. H., et al. 1997, *Sol. Phys.*, 170, 63
- Fisher, G. H., Bercik, D. J., Welsch, B. T., & Hudson, H. S. 2012, *Sol. Phys.*, 277, 59
- Fisher, G. H., Canfield, R. C., & McClymont, A. N. 1985a, *ApJ*, 289, 434
- Fisher, G. H., Canfield, R. C., & McClymont, A. N. 1985b, *ApJ*, 289, 425
- Fisher, G. H., Canfield, R. C., & McClymont, A. N. 1985c, *ApJ*, 289, 414
- Green, L. M., Valori, G., Zuccarello, F. P., et al. 2017, *ApJ*, 849, 40
- Hansen, S. C., Cally, P. S., & Donea, A.-C. 2016, *MNRAS*, 456, 1826
- Hochedez, J.-F., Schmutz, W., Stockman, Y., et al. 2006, *Advances in Space Research*, 37, 303
- Holman, G. D., Aschwanden, M. J., Aurass, H., et al. 2011, *Space Sci. Rev.*, 159, 107
- Houdebine, E. R. & Doyle, J. G. 1994, *A&A*, 289, 185
- Houdebine, E. R., Foing, B. H., & Rodono, M. 1990, *A&A*, 238, 249
- Hudson, H., Fisher, G., & Welsch, B. 2008, in *Astronomical Society of the Pacific Conference Series*, Vol. 383,

- Subsurface and Atmospheric Influences on Solar Activity, ed. R. Howe, R. Komm, K. Balasubramaniam, & G. Petrie, 221
- Ichimoto, K. & Kurokawa, H. 1984, *Sol. Phys.*, 93, 105
- Inoue, S., Shiota, D., Bamba, Y., & Park, S.-H. 2018, *ApJ*, 867, 83
- Kaempfer, N. & Magun, A. 1983, *ApJ*, 274, 910
- Kawate, T., Keenan, F. P., & Jess, D. B. 2016, *ApJ*, 826, 3
- Kleint, L., Heinzl, P., Judge, P., & Krucker, S. 2016, *ApJ*, 816, 88
- Kontar, E. P., Brown, J. C., Emslie, A. G., et al. 2011, *Space Sci. Rev.*, 159, 157
- Kosovichev, A. 2011, arXiv preprint arXiv:1103.1707
- Kosovichev, A. G. & Zharkova, V. V. 1998, *Nature*, 393, 317
- Kotrč, P., Procházka, O., & Heinzl, P. 2016, *Sol. Phys.*, 291, 779
- Kurokawa, H., Takakura, T., & Ohki, K. 1988, *PASJ*, 40, 357
- Lin, R. P., Dennis, B. R., Hurford, G. J., et al. 2002, *Sol. Phys.*, 210, 3
- Lindsey, C. & Braun, D. 2000, *solphys*, 192, 261
- Lindsey, C. & Braun, D. 2004, *ApJS*, 155, 209
- Lindsey, C. & Braun, D. C. 1999, *ApJ*, 510, 494
- Liu, C., Deng, N., Lee, J., et al. 2014, *Apj*, 795, 128
- Lysenko, A. L., Anfinogentov, S. A., Svinkin, D. S., Frederiks, D. D., & Fleishman, G. D. 2019, *ApJ*, 877, 145
- Machado, M. E., Milligan, R. O., & Simões, P. J. A. 2018, *ApJ*, 869, 63
- Macrae, C., Zharkov, S., Zharkova, V., et al. 2018, *A&A*, 619, A65
- Matthews, S. A., Harra, L. K., Zharkov, S., & Green, L. M. 2015, *ApJ*, 812, 35
- Matthews, S. A., Zharkov, S., & Zharkova, V. V. 2011, *ApJ*, 739, 71
- Milligan, R. O. & Dennis, B. R. 2009, *ApJ*, 699, 968
- Milligan, R. O., Gallagher, P. T., Mathioudakis, M., et al. 2006a, *ApJ*, 638, L117
- Milligan, R. O., Gallagher, P. T., Mathioudakis, M., & Keenan, F. P. 2006b, *ApJ*, 642, L169
- Moradi, H., Donea, A.-C., Lindsey, C., Besliu-Ionescu, D., & Cally, P. S. 2007, *MNRAS*, 374, 1155
- Polito, V., Reep, J. W., Reeves, K. K., et al. 2016, *ApJ*, 816, 89
- Porquet, D., Arnaud, M., & Decourchelle, A. 2001, *A&A*, 373, 1110
- Priest, E. & Forbes, T. 2000, *Magnetic Reconnection* (Cambridge University Press)
- Procházka, O., Milligan, R. O., Allred, J. C., et al. 2017, *ApJ*, 837, 46
- Procházka, O., Reid, A., Milligan, R. O., et al. 2018, *ApJ*, 862, 76
- Quinn, S., Reid, A., Mathioudakis, M., et al. 2019, *ApJ*, accepted
- Radziszewski, K., Rudawy, P., & Phillips, K. J. H. 2011, *A&A*, 535, A123
- Romano, P., Elmhamdi, A., Falco, M., et al. 2018, *ApJ*, 852, L10
- Scharmer, G. B. 2006, *A&A*, 447, 1111
- Scharmer, G. B., Dettori, P. M., Lofdahl, M. G., & Shand, M. 2003, in *Society of Photo-Optical Instrumentation Engineers* (SPIE) Conference Series, Vol. 4853, *Innovative Telescopes and Instrumentation for Solar Astrophysics*, ed. S. L. Keil & S. V. Avakyan, 370–380
- Sharykin, I. N. & Kosovichev, A. G. 2018, *ApJ*, 864, 86
- Sharykin, I. N., Kosovichev, A. G., & Zimovets, I. V. 2015, *ApJ*, 807, 102
- Somov, B. V., ed. 2000, *Astrophysics and Space Science Library*, Vol. 251, *Cosmic Plasma Physics* (Springer Verlag)
- Somov, B. V., Spektor, A. R., & Syrovatskii, S. I. 1981, *Sol. Phys.*, 73, 145
- Syrovatskii, S. I. & Shmeleva, O. P. 1972, *Soviet Astronomy*, 16, 273
- Uchida, Y. & Hudson, H. 1972, *Sol. Phys.*, 26, 414
- Veronig, A., Vršnak, B., Temmer, M., & Hanslmeier, A. 2002, *Sol. Phys.*, 208, 297
- Vilmer, N., MacKinnon, A. L., & Hurford, G. J. 2011, *Space Sci. Rev.*, 159, 167
- Wuelser, J.-P. & Marti, H. 1989, *ApJ*, 341, 1088
- Zarro, D. M., Canfield, R. C., Metcalf, T. R., & Strong, K. T. 1988, *ApJ*, 324, 582
- Zhao, J. & Chen, R. 2018, *ApJ*, 860, L29
- Zharkov, S. 2013, *Monthly Notices of the Royal Astronomical Society*, 431, 3414
- Zharkov, S., Green, L., Matthews, S., & Zharkova, V. 2011b, *ApJ*, 741, L35
- Zharkov, S., Green, L., Matthews, S., & Zharkova, V. 2013a, *Journal of Physics Conference Series*, 440, 12046
- Zharkov, S., Green, L. M., Matthews, S. A., & Zharkova, V. V. 2013b, *Sol. Phys.*, 284, 315
- Zharkov, S., Zharkova, V. V., & Matthews, S. A. 2011a, *ApJ*, 739, 70
- Zharkova, V. & Kobylinskii, V. 1993, *Sol. Phys.*, 143, 259
- Zharkova, V. & Zharkov, S. 2007, *ApJ*, 664, 573
- Zharkova, V. & Zharkov, S. 2015, *Sol. Phys.*, 290, 3163
- Zharkova, V. V. 2008, *Sol. Phys.*, 251, 641
- Zharkova, V. V., Arzner, K., Benz, A. O., et al. 2011, *Space Sci. Rev.*, 159, 357
- Zharkova, V. V. & Gordovskyy, M. 2006, *ApJ*, 651, 553
- Zharkova, V. V., Zharkov, S. I., Druett, M., Matthews, S. A., & Inoue, S. 2020, , Paper 2, in press

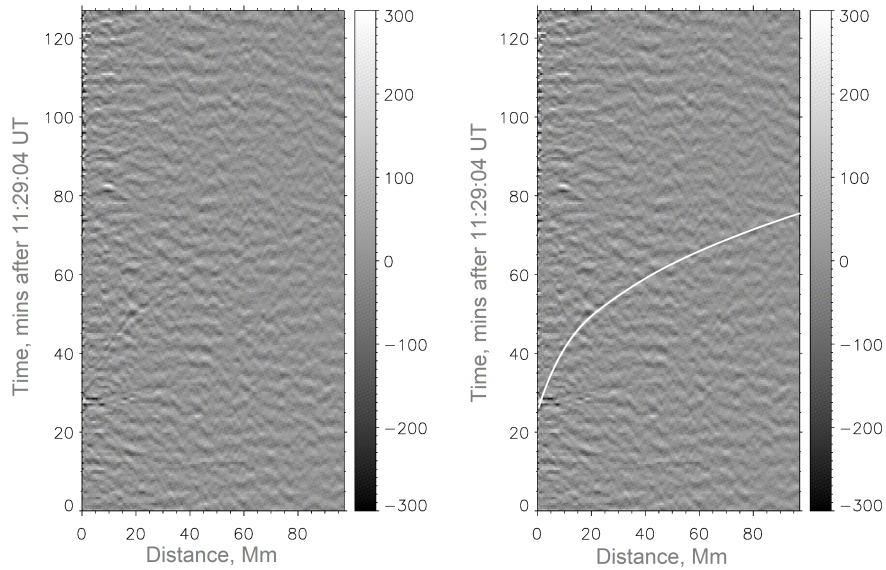


Fig. 6. Time–distance diagram for seismic source 1 obtained from the filtered HMI dopplergram without (left) and with theoretical curve (right) showing the acoustic wave ridge. The start (zero) time on the Y-axis is 11:29.04 UT, leading to the seismic response start at 11:55:37 UT. The grey colour bars on the right show the background Doppler velocities in m/s.

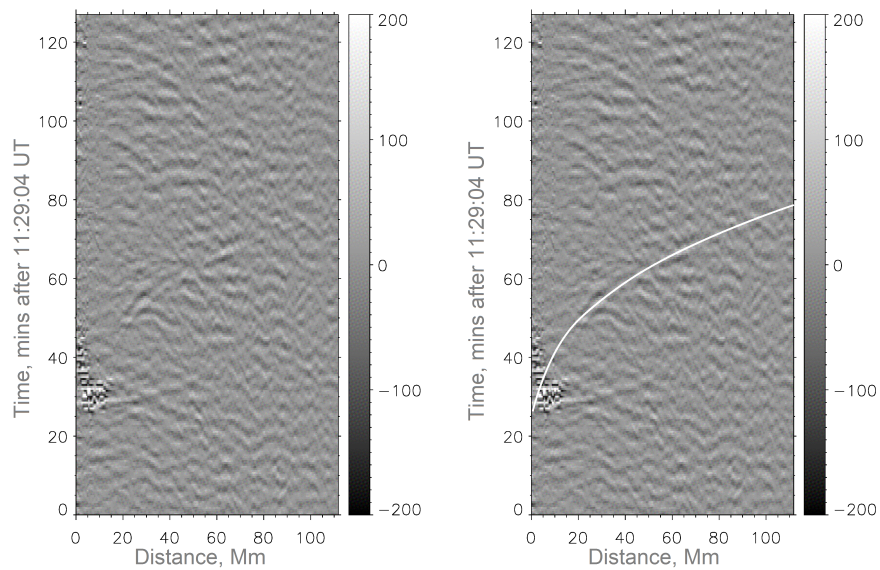


Fig. 7. Time–distance diagram for seismic source 3 obtained from the filtered HMI dopplergram without (left) and with theoretical curve (right) showing the acoustic wave ridge. The start (zero) time on the Y-axis is 11:29.04 UT, leading to the seismic response start at 11:55:37 UT. The grey colour bars on the right show the background Doppler velocities in m/s.

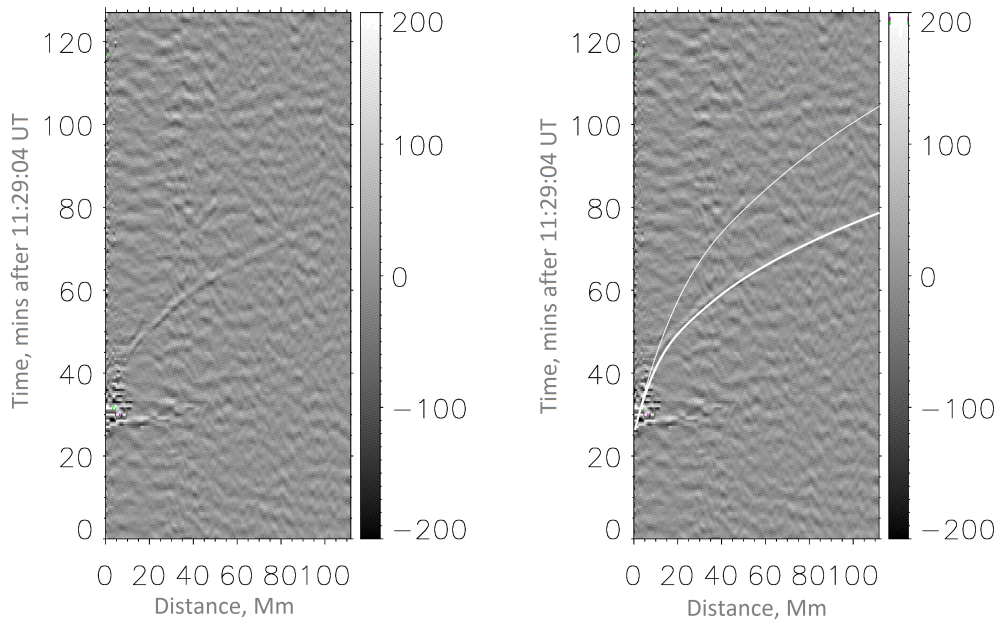


Fig. 8. Time–distance diagram for the seismic source 2, obtained from the filtered HMI dopplergram without (left) and with (right) theoretical curves. The TD diagram shows the ridge derived from ripples produced at some distance from the event location by acoustic waves in their first bounce from the photosphere (lower white line) and the second bounce (upper white line). The start (zero) time on the Y-axis is 11:29.04 UT, which corresponds to the shock deposition and seismic response initiation at 11:55:37 UT. The grey colour bars on the right show the background Doppler velocities in m/s.

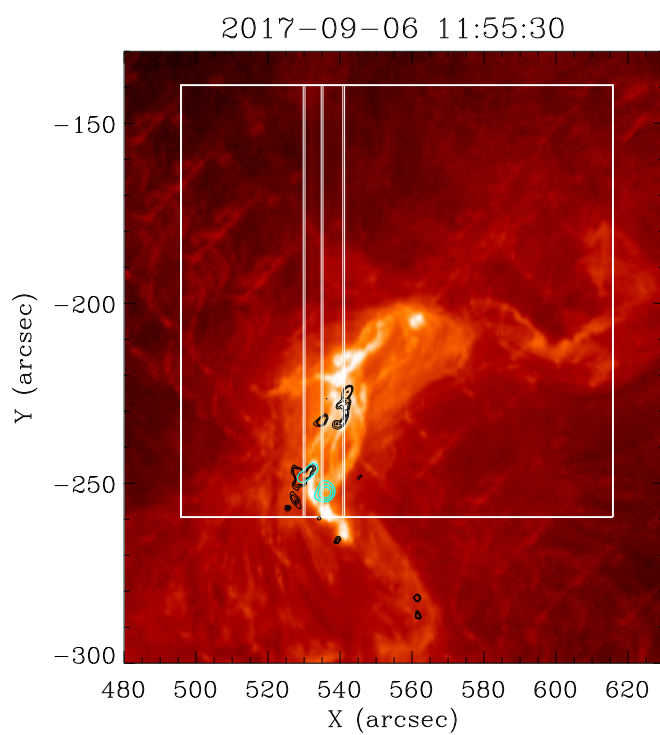


Fig. 9. AIA He II 304 image showing the EIS FOV (white box); the 6 mHz egression contours (black) and the 30-60 keV HXR emission (cyan contours) obtained at 12:08:26 UT. The white vertical lines indicate the location of the EIS slits with respect to the main egression sources within the EIS FOV.

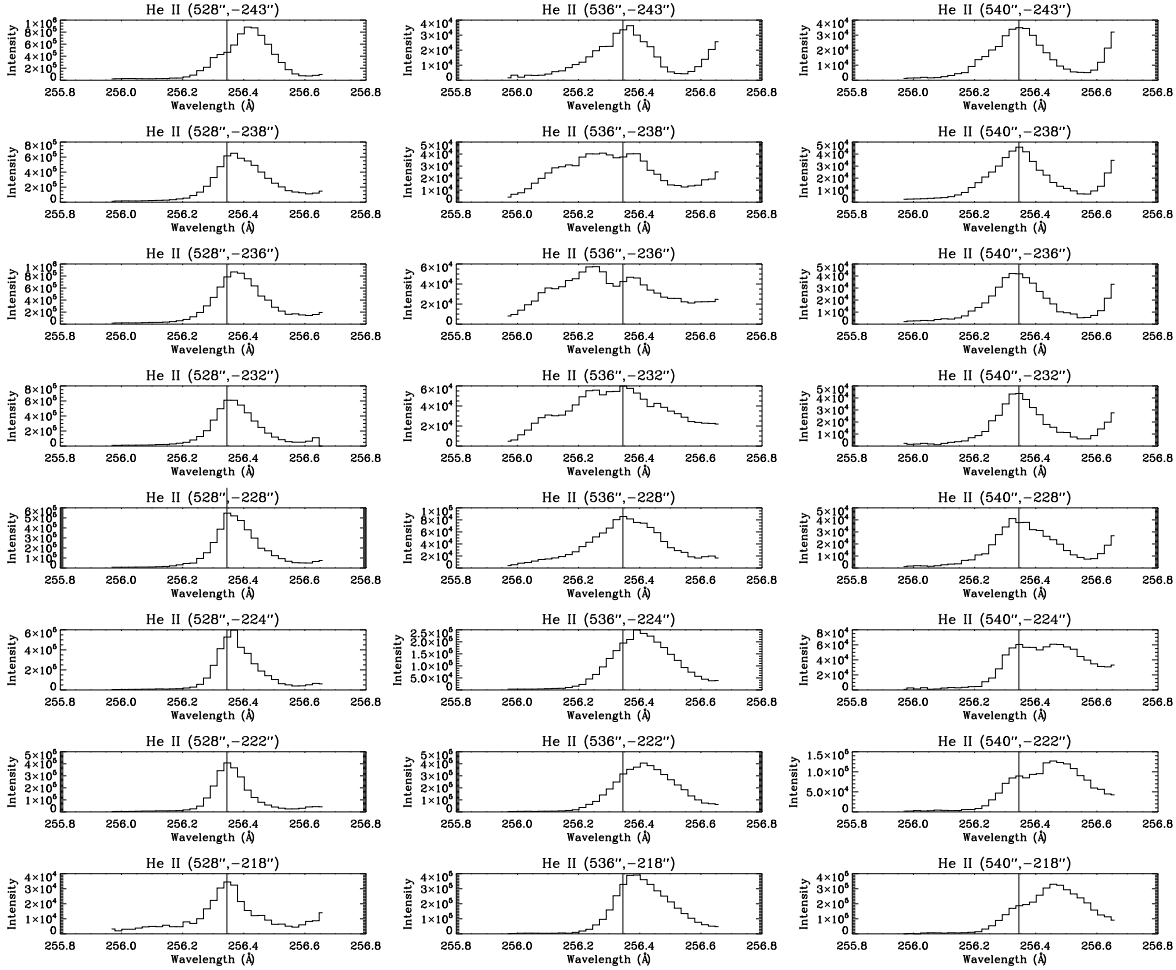


Fig. 10. Flaring event 1 (>11:55 UT): EIS He II line profiles from the selected locations at the slit positions associated with the locations of seismic sources (SQs) 1, 2, and 3. Heliocentric location is indicated above each profile. The vertical lines indicate the rest wavelength.

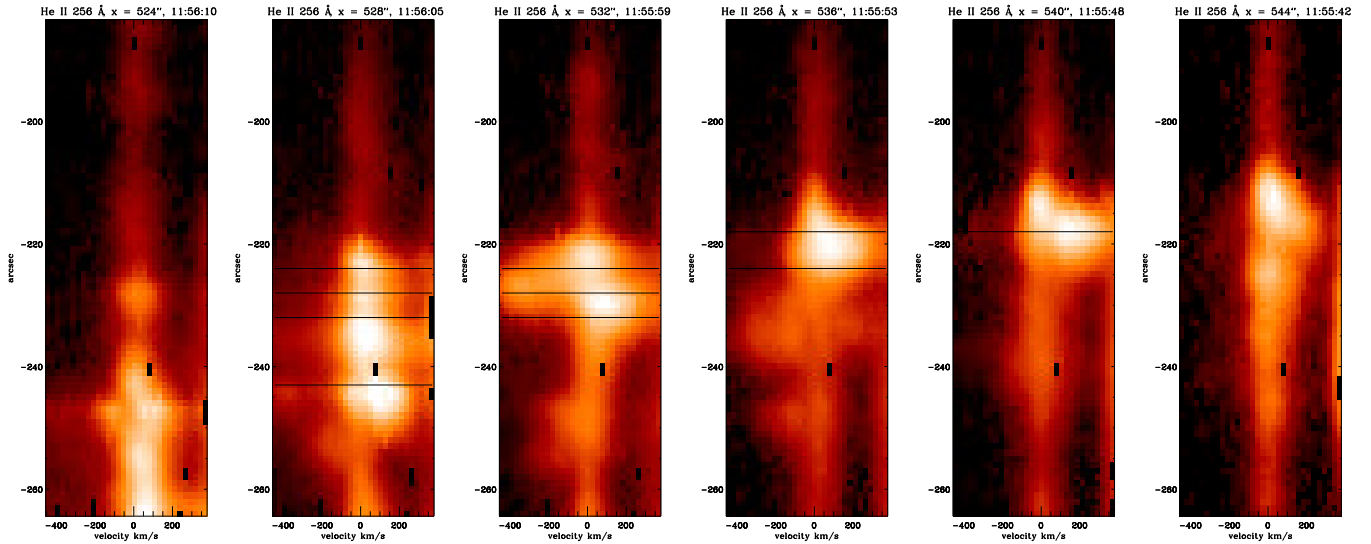


Fig. 11. Flaring event 1 (>11:55 UT): Series of EIS spectrograms in the He II 256 Å line taken during the onset phase of the X9.3 flare on 6 September 2017. The titles above spectrograms indicate the time and slit location, while the y-axis represents location along the slit, and Doppler velocities represented on the x-axis. Black horizontal lines indicate the location of the egression sources (sunquakes and some others, which were later disregarded as SQs).

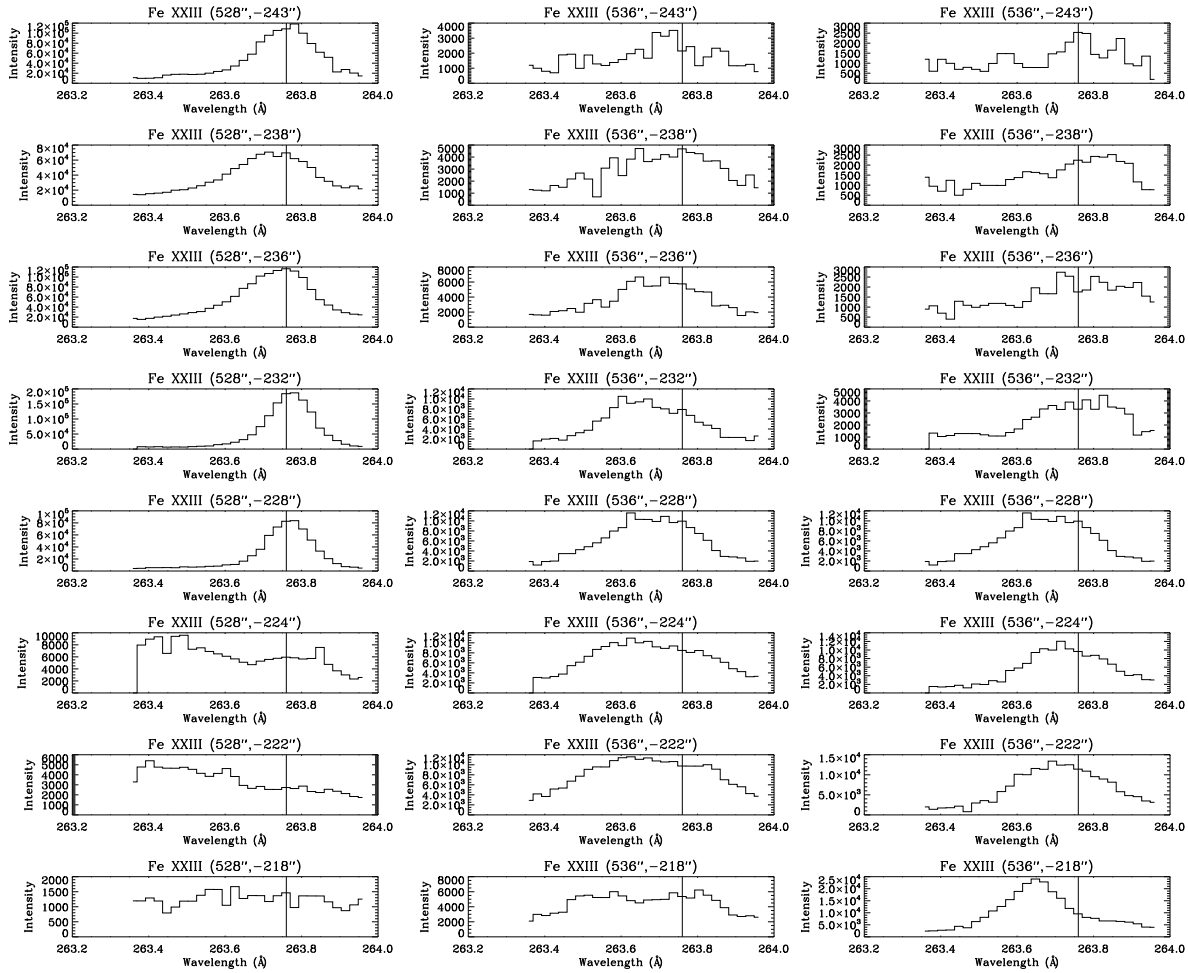


Fig. 12. Flaring event 1 ($>11:55$ UT): EIS Fe XXIII line profiles from the selected locations at the slit positions associated with the locations of SQs 1, 2, and 3. Heliocentric location is indicated above each profile. The vertical lines indicate the rest wavelength.

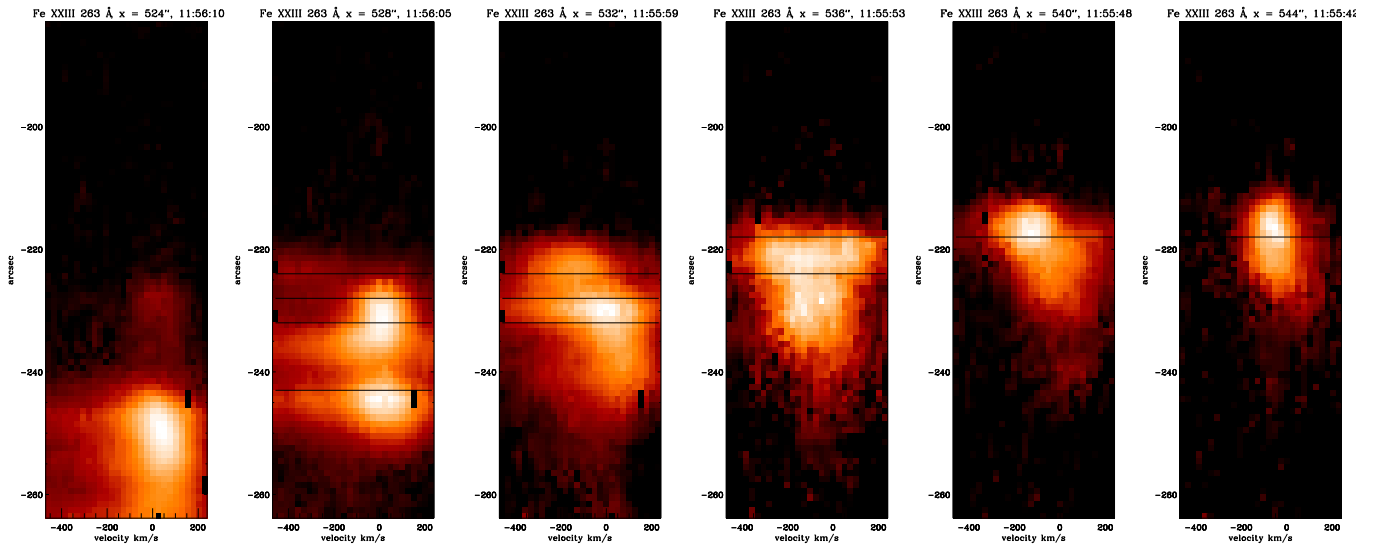


Fig. 13. Flaring event 1 ($>11:55$ UT): Series of EIS spectrograms in the Fe XXIII 263.76 \AA line taken during the onset phase of the X9.3 flare on 6 September 2017. The titles above spectrograms indicate the time and slit location, while the y-axis represents location along the slit, and Doppler velocities represented on the x-axis. Black horizontal lines indicate the location of the egression sources.

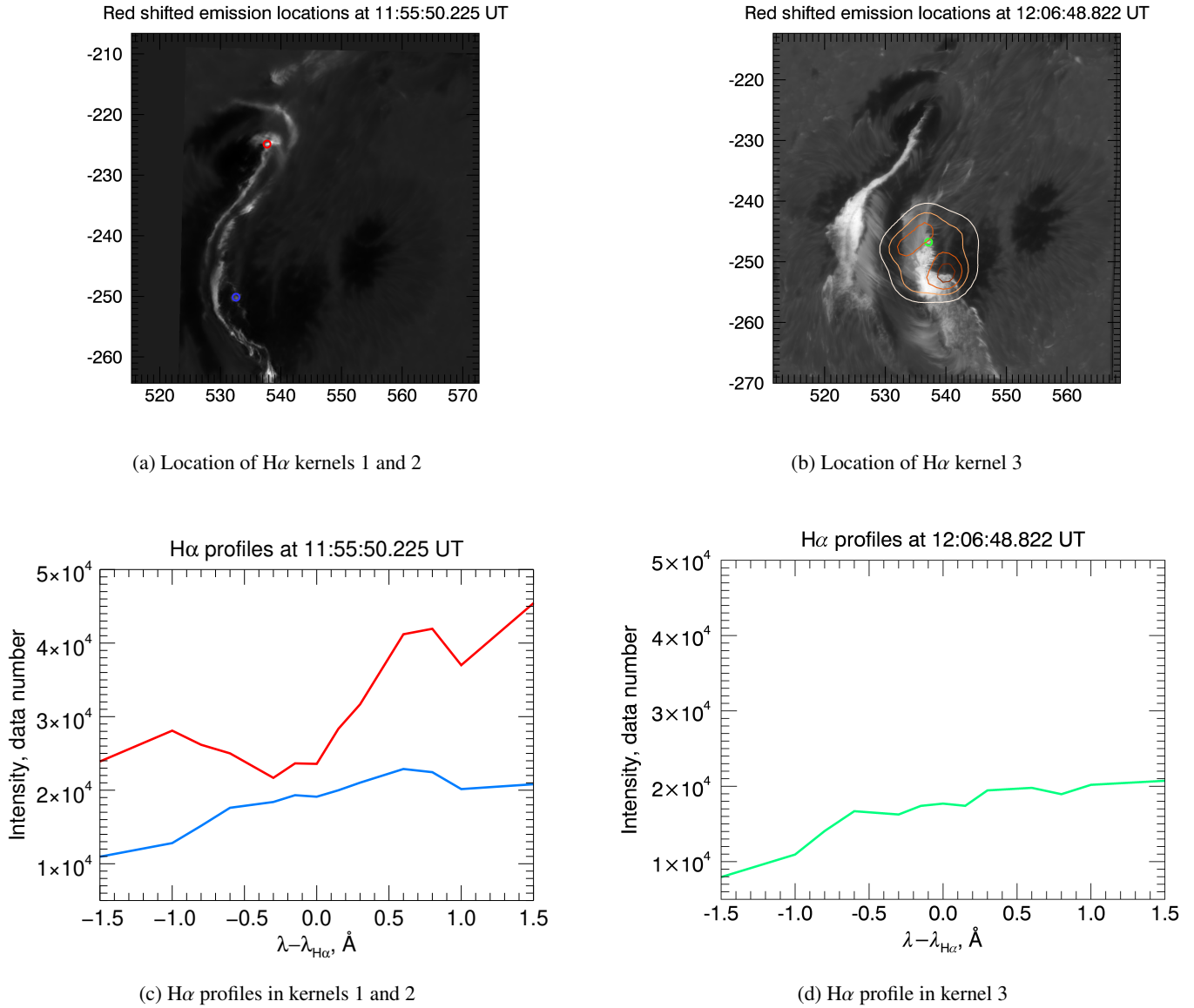


Fig. 14. Top plots: Red wing emission ($\lambda_{H\alpha} + 1.5 \text{ \AA}$) in the H α line at 11:55:50 UT (flaring event 1) with the locations of (a) kernel 1 (seismic source 1) and kernel 2 (seismic source 2), shown by the red and blue circles, respectively, and the location of (b) kernel 3 (flaring event 2), marked by the green circle, observed at 12:06:48 UT. Bottom plots: (c) H α line profiles in kernel 1 (red line) and kernel 2 (blue line) and (d) kernel 3 (green line) obtained with SST (arbitrary units) by taking the average over the pixels. The HXR contours obtained at 12:08:26 UT are over-plotted for the 25-50 keV channel with the contours at 0.25 of maximal intensity (white), 0.48 (light brown), 0.7 (medium brown), and 0.9 (dark brown).

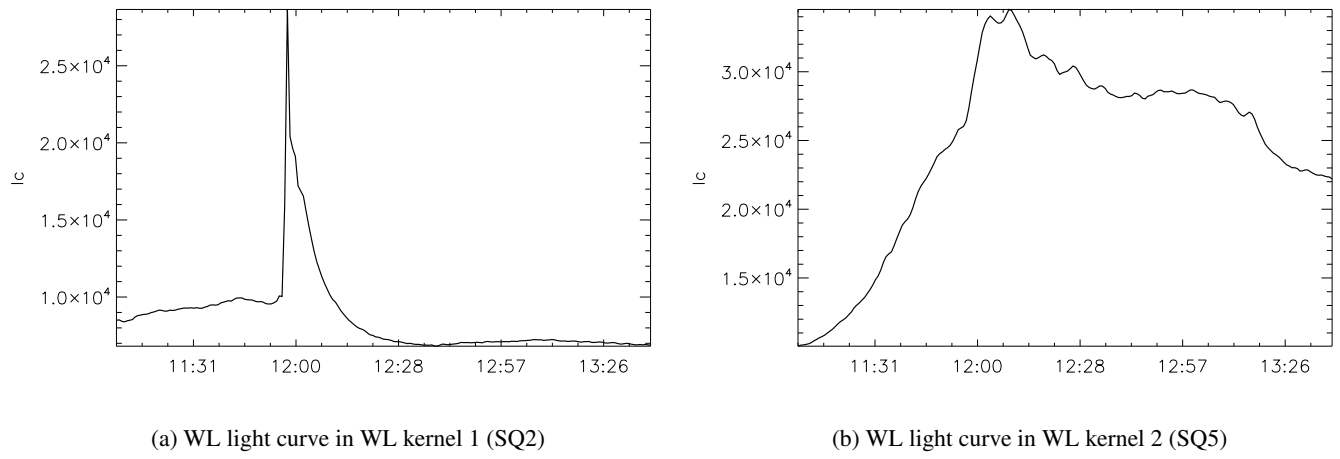


Fig. 15. (a) Temporal profiles of white light emission obtained in the WL kernel 1 in the locations of the $H\alpha$ kernels 2 and seismic source 2, and (b) WL light curve in kernel 2 at the location of $H\alpha$ kernel 3 and possible seismic source 5.